

This is the accepted manuscript made available via CHORUS. The article has been published as:

Turbulence in a hypersonic compression ramp flow

Stephan Priebe and M. Pino Martín

Phys. Rev. Fluids **6**, 034601 — Published 2 March 2021

DOI: [10.1103/PhysRevFluids.6.034601](https://doi.org/10.1103/PhysRevFluids.6.034601)

Turbulence in a hypersonic compression ramp flow

Stephan Priebe* and M. Pino Martín

Department of Aerospace Engineering,

University of Maryland, College Park MD 20742

(Dated: January 14, 2021)

Abstract

A hypersonic shock wave/turbulent boundary layer interaction (STBLI) is investigated using direct numerical simulation (DNS). The geometry is an 8° compression ramp, and the flow conditions upstream of the interaction are Mach 7.2 and $Re_\theta = 3500$. Consistent with experiments at similar conditions, the flow is found to be attached in the mean, although the DNS shows that the probability of observing reversed flow on an instantaneous basis is significant. Due to the high Mach number of the flow combined with a low deflection angle, the shock angle is shallow and the shock is immersed in the boundary layer for a streamwise distance equal to several incoming boundary layer thicknesses downstream of the compression corner. The instantaneous flow structure observed in the DNS is in good qualitative agreement with filtered Rayleigh scattering images obtained experimentally that are available in the literature. The behavior of the turbulence is described based on the evolution of the Reynolds stresses, the anisotropy tensor, the wall pressure spectra, and the TKE budget through the interaction. The various Reynolds stress components are found to be amplified by factors of 1.8 to 2.5. The heat transfer through the interaction is also investigated, as well as the relationship between the velocity and temperature fields. At the corner and for a significant distance downstream of the corner, the Reynolds Analogy factor lies above values typically observed in zero pressure gradient hypersonic boundary layers. A common heat transfer-pressure scaling describes the behavior observed in the DNS more accurately but with some departures near the corner. In the present attached STBLI, the strong Reynolds analogy (SRA), including the assumption of a constant turbulent Prandtl number around unity, is satisfied reasonably well in the interaction, although there are significant departures in the near-wall region.

INTRODUCTION

While the turbulence in trans- and supersonic shock wave/turbulent boundary layer interactions (STBLIs) has been studied extensively, there are only a few studies of the turbulence in hypersonic interactions, at Mach numbers greater than 5.

Mikulla & Horstman [1] performed two-component hot-wire measurements in Mach 7 axisymmetric, reflected STBLIs. The boundary layer developed on a centerbody that consisted of a conical forebody followed by a circular cylinder, and the shock was generated by an outer, concentric cowl. Two shock generator angles (7.5° and 15°) were considered, which resulted in attached and separated flow, respectively. The streamwise and wall-normal fluctuating velocities were measured, and the Reynolds shear stress was calculated based on the measurements. It was found that the turbulence was significantly amplified in the attached case and that the fluctuation peak moved away from the wall as is typically observed in adverse pressure gradient flows, whereas the separated case showed significant amplification only in the vicinity of the shock, downstream of which the turbulence fluctuations rapidly returned to equilibrium levels. Bookey et al. [2] studied an 8° compression ramp STBLI at Mach 7.2. In addition to investigating the time-averaged flow, they also investigated the instantaneous turbulent flow structure using filtered Rayleigh scattering (FRS). The case is attached in the mean, and the shock was found to be shallow, so that the shock foot was immersed in the boundary layer for a streamwise distance equal to several incoming boundary layer thicknesses downstream of the corner. The FRS images showed that on an instantaneous basis the shock was strongly distorted by the turbulent eddies. Schreyer et al. [3, 4] performed particle image velocimetry (PIV) measurements for the same Mach 7.2, 8° compression ramp case that was investigated by Bookey. The PIV results showed that the wall-normal velocity fluctuations are significantly amplified through the interaction, whereas the streamwise fluctuations are only weakly amplified. As expected in adverse pressure gradient flows, the fluctuation peak moved away from the wall as had also been observed by Mikulla & Horstman [1]. Further examples of the application of PIV to hypersonic STBLI are Schrijer, Scarano & van Oudheusden [5], who investigated a Mach 7 double ramp flow, and Brooks et al. [6], who investigated a hollow cylinder with flare at Mach 10.

Most experiments of hypersonic STBLIs do not include turbulence measurements. Surface quantities such as the wall pressure and heat transfer are typically measured (skin friction

measurements are rarer), together with mean-flow visualizations such as Schlieren images, and mean flow surveys (see Elfstrom [7], Coleman & Stollery [8], Kussoy & Horstman [9–11], Holden [12, 13], Holden et al. [14, 15], Schülein [16], Murray, Hillier & Williams [17], among others). These works show that the surface heat transfer is significantly amplified through the interaction, which is an important consideration in high-speed flight applications. The relationships between the temperature and velocity field that are valid in attached, zero pressure gradient boundary layers break down in hypersonic STBLIs. According to the Reynolds analogy (RA), the surface heat transfer coefficient, C_h , scales with the skin-friction coefficient, C_f : $RAF = \frac{2C_h}{C_f} = const. \approx 1$. This relationship is satisfied relatively closely in undisturbed hypersonic boundary layers. In hypersonic STBLIs, however, significant departures from the RA are observed (e.g. Schülein [16]). The surface heat flux appears to scale with pressure, rather than skin friction, and several such scalings have been proposed (Back & Cuffel [18], Coleman & Stollery [8]) and shown to match experiments (e.g. Holden [12], Murray et al. [17]). A review of heat transfer in STBLI may be found in Gaitonde [19].

Hypersonic STBLIs are difficult to predict accurately using common Reynolds-averaged Navier–Stokes (RANS) methods. Predictions obtained with standard turbulence models give significant errors compared to experimental data, not only for separated cases but also for attached ones. Roy & Blottner [20] reviewed hypersonic experiments and computations. They concluded that the heat transfer is particularly difficult to predict and is ‘often in error by a factor of four or more’ [20]. Gnoffo et al. [21] assessed the prediction accuracy of standard turbulence models for hypersonic compression ramp interactions. They introduced an uncertainty metric that captures the total error of the CFD prediction compared to reference experimental data based on the error in the three surface quantities that are typically available from experiment: the wall pressure distribution, the surface heat transfer and the length of the separated flow. Their uncertainty metric is 55% for cases with mean-flow separation and 25% for cases without mean-flow separation [21]. High levels of error are similarly found in predictions of reflected shock interactions, see Brown [22]. Note that prediction errors are present not only for turbulent hypersonic shock/boundary layer interactions but also for laminar ones (e.g. Knight & Mortazavi [23]).

One of the contributing reasons for the turbulence model deficiencies is the limited number of available experiments and numerical simulations that are suitable for model development and detailed validation. Settles & Dodson [24–26] reviewed super- and hypersonic STBLI

experiments and identified 19 experiments suitable for model development and validation, of which 7 are in the hypersonic regime. The more recent review by Roy & Blottner [20] identified nine experiments. These experiments include measurements of mean surface quantities, such as the wall pressure and heat transfer, and as discussed in Roy & Blottner [20] and Gnoffo et al. [21], off-wall and turbulence quantities, which would be useful for model development, are usually not available.

In the present work, we describe the direct numerical simulation (DNS) of an attached hypersonic compression ramp STBLI. The behavior of the turbulence through the interaction is analyzed. The heat transfer as well as the mean and fluctuating temperature field are also investigated, and standard relationships between the temperature and velocity field are assessed. We expect that the present DNS data set, which provides off-wall and turbulence quantities, may be used for developing and validating RANS and LES models, with the aim of improving predictions of hypersonic STBLI.

The paper is organized as follows: the numerical method and computational setup are presented in § . The results for the undisturbed upstream boundary layer are discussed in § and the results for the compression ramp interaction in § . A summary with conclusions is given in § .

NUMERICAL METHODS AND COMPUTATIONAL SETUP

The DNS code solves the compressible Navier–Stokes equations using the following numerical scheme: an optimized WENO scheme [27, 28] is used for the discretization of the convective fluxes, standard fourth-order central differences for the discretization of the viscous fluxes, and a third-order low-storage Runge–Kutta scheme [29] for time integration.

The present flow conditions are low-enthalpy conditions typical of ground-based test facilities. At these low-enthalpy conditions, air behaves as a perfect gas, and we thus use the perfect gas law $p = \rho RT$ with constant specific heats. The dynamic viscosity μ is calculated using Keyes' law $\mu = 1.488 \times 10^{-6} \frac{\sqrt{T}}{1 + (122.1/T)10^{-5/T}}$, where T is the temperature (in Kelvin) and μ is in Pa s [30]. Keyes' law and the commonly-used Sutherland's law are compared in figure 1 for the range of temperatures encountered in the present flow. There are significant differences between the two viscosity models for $T < 100K$. Since $T_\infty = 62.9K$ in the present flow, we use Keyes' law, which is more accurate at these low temperatures

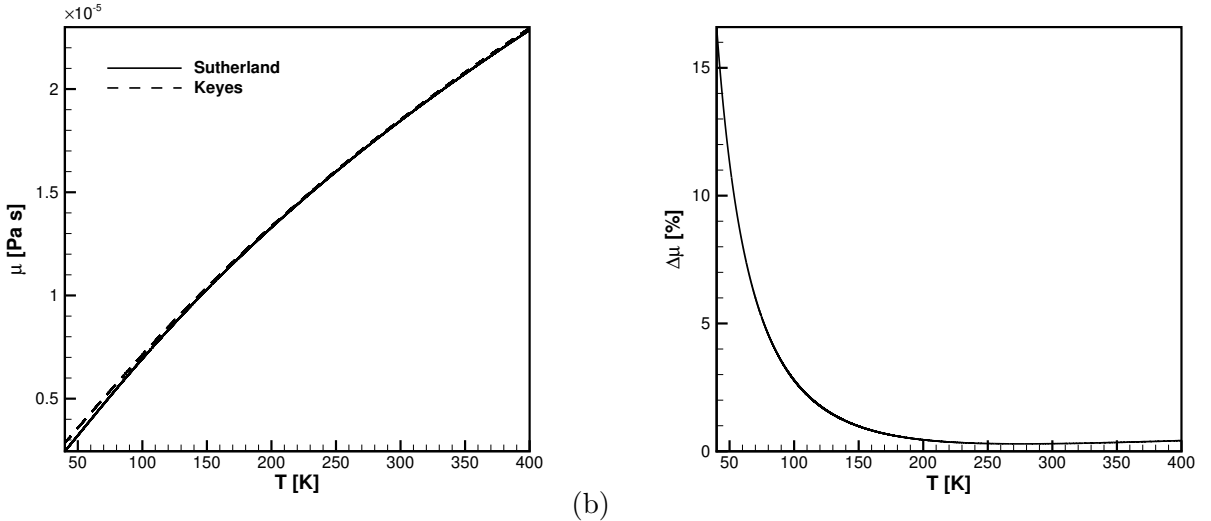


FIG. 1. Comparison between Sutherland’s and Keyes’ viscosity model: (a) model-predicted viscosity vs. temperature, and (b) relative difference between the two models, $\Delta\mu = \frac{\mu_{Keyes} - \mu_{Sutherland}}{\mu_{Sutherland}}$, vs. temperature.

(see Roy & Blottner [20]). We note, however, that the temperature increases as the wall is approached where $T_w = 340K$. The viscous stresses are largest in the near-wall region, which is at sufficiently high temperatures that the difference between the two viscosity models is small. The choice of viscosity model is thus expected to only affect the outer region of the boundary layer and the freestream, where viscous stresses tend to be small. Nevertheless, Keyes’ law is more appropriate at the present conditions and is thus used in the DNS.

Regarding the computational setup, two simulations are run: (1) an undisturbed, zero-pressure-gradient, spatially-developing boundary layer (auxiliary DNS), and (2) an 8° compression ramp (principal DNS). The inflow boundary condition for the principal DNS is extracted from a spanwise-wall normal plane of the auxiliary DNS.

The domain size for the auxiliary DNS is $L_x = 27\delta_{ref}$ in the streamwise direction, $L_y = 10\delta_{ref}$ in the spanwise direction, and $L_z = 14.2\delta_{ref}$ in the wall-normal direction, where $\delta_{ref} = 5mm$ is (approximately) equal to the boundary layer thickness at the inlet of the principal DNS. The domain is discretized with $N_x = 840$, $N_y = 768$, and $N_z = 150$ grid points for a total of 97 million. The grid resolutions based on the flow quantities at the inlet are $\Delta x^+ = 7.5$, $\Delta y^+ = 3.0$ and the first grid point from the wall is at $z^+ = 0.26$.

The domain size for the principal DNS is $L_x \approx 22.5\delta_{ref}$ (the corner is at $12\delta_{ref}$ from the

inlet), $L_y = 10\delta_{ref}$, and $L_z \approx 9\delta_{ref}$, discretized with $N_x = 1060$, $N_y = 768$, and $N_z = 170$ grid points for a total of 138 million. The grid resolutions in the streamwise and spanwise directions are $\Delta x^+ = 7.0$ (inlet) to 3.2 (corner), and $\Delta y^+ = 2.8$; the first grid point from the wall is at $z^+ = 0.19$, and the resolution at the boundary layer edge is $\Delta z/\delta_{ref} = 0.036$.

Both the principal and auxiliary DNS use an isothermal, no-slip boundary condition at the wall ($T_w = 340K$, which matches the reference experiments [4]), a periodic boundary condition in the span, and an extrapolation boundary condition at the top and outlet boundaries. The inlet boundary condition for the auxiliary DNS is specified using the rescaling method of Xu & Martín [31]; the recycling station is located at $x/\delta_{ref} = 26.0$ from the domain inlet. A time series of the flow at the recycling station is saved and used as the inflow boundary condition for the principal DNS.

Except for the change in the viscosity model described above, the present code is identical to the one that has been used in previous supersonic STBLI studies [32–34]. The same numerical approach has also been used in super- and hypersonic boundary layer studies [35–37]. In these previous works, the code has been validated against experiments and known analytical correlations. In addition, the present DNS is at similar conditions as the experiments by Bookey et al. [2] and Schreyer et al. [4]. Comparison to these experiments is made in the results section and good overall agreement is observed. The data used for comparison includes instantaneous flow visualizations, mean flow visualizations (Schlieren), and oil-flow visualizations. A comparison between PIV data and the DNS may be found in Schreyer et al. [4].

The boundary layer DNS uses similar grid resolutions as in previous hypersonic boundary layer calculations [35], and the STBLI DNS uses similar grid resolutions as in previous supersonic calculations [32]. In addition, a grid convergence study for the present STBLI DNS has been performed (Priebe [38]), which shows that the results are converged except for a small sensitivity near the exit of the domain. In the last $3 - 4\delta_{ref}$ in the streamwise direction, C_f is higher on some of the refined grids compared to the baseline by up to 4%. In this region, the grid is somewhat coarser for two reasons: the first is that the grid is stretched in the streamwise direction towards the exit, and the second is that the wall unit $\nu_w/u_\tau = \mu_w/\sqrt{\rho_w\tau_w}$ decreases across the interaction (since both ρ_w and τ_w increase). Based on local wall units, the resolutions at a few representative locations on the ramp are: $\Delta x^+ = 8$, $\Delta y^+ = 6$, and $z^+ = 0.41$ at $x/\delta_{ref} = 2$; $\Delta x^+ = 11$, $\Delta y^+ = 7$, and $z^+ = 0.47$ at

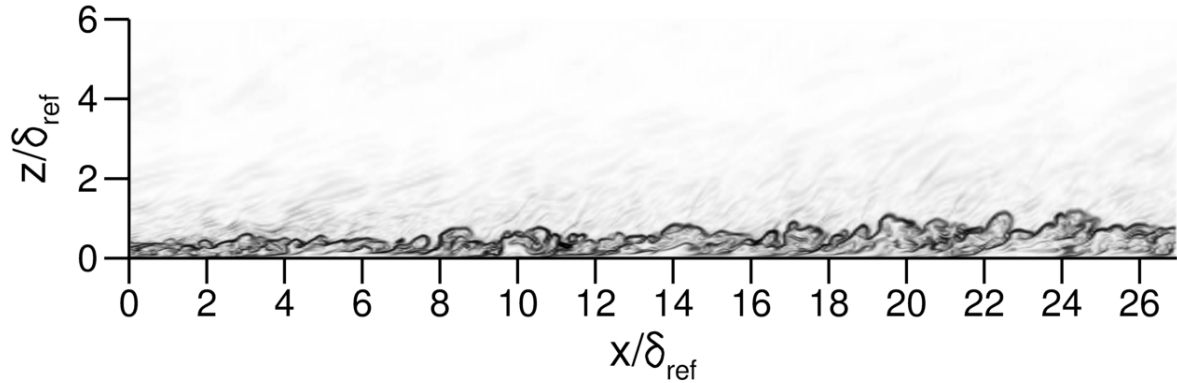


FIG. 2. Numerical Schlieren visualization of the Mach 7.2, zero-pressure-gradient boundary layer (auxiliary DNS).

$x/\delta_{ref} = 5$; $\Delta x^+ = 18$, $\Delta y^+ = 8$, and $z^+ = 0.53$ at $x/\delta_{ref} = 10$ (just upstream of the exit). Detailed results, such as profiles of fluctuating quantities, strong Reynolds analogy terms, and TKE budgets, are only shown up to $x/\delta_{ref} = 6$ in the present paper, thus excluding the region near the exit where a grid sensitivity, although small, has been observed.

RESULTS

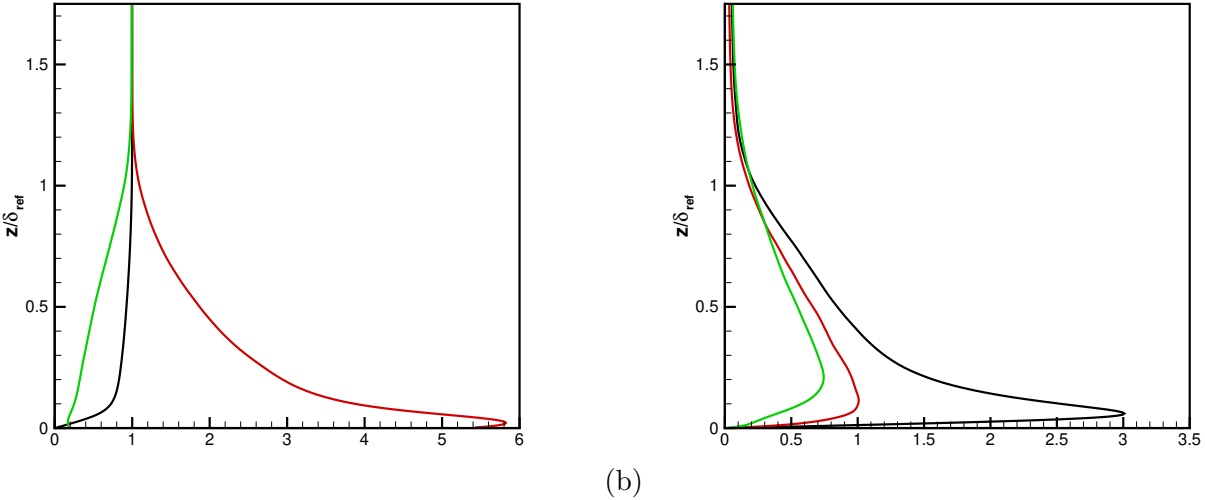
Upstream boundary layer

Figure 2 shows a typical instantaneous visualization of the auxiliary DNS. The variable plotted here and also in figure 7 is a nonlinear function of the density gradient magnitude, $e^{-10|\nabla\rho|/|\nabla\rho|_{ref}}$, which gives Schlieren-like visualizations and has been used previously (e.g. [32, 34, 37]). The value of $|\nabla\rho|_{ref}$ is adjusted here to be representative of large instantaneous values of $|\nabla\rho|$ encountered in the domain which then appear as dark regions in the visualizations. As is apparent from figure 2, the boundary layer grows significantly over the streamwise length of the domain. The boundary layer thickness increases from $\delta/\delta_{ref} = 0.45$ at the inlet to 0.925 at the outlet. The momentum thickness increases from $\theta/\delta_{ref} = 0.0175$ at the inlet to 0.0355 at the outlet, and consequently the momentum-thickness Reynolds number increases from $Re_\theta = 1650$ to 3350. The displacement thickness increases from $\delta^*/\delta_{ref} = 0.245$ to 0.5.

The flow conditions are listed in table I, where the boundary layer quantities have been

TABLE I. Flow conditions.

M_∞	Re_θ	δ^+	δ [mm]	δ^* [mm]	θ [mm]	U_∞ [m/s]	u_τ [m/s]	p_∞ [Pa]	T_∞ [K]
7.21	3.3×10^3	2.1×10^2	4.58	2.48	0.175	1146.1	62.5	1341.0	62.9


 FIG. 3. Upstream boundary layer profiles. (a) $\bar{\rho}$ (green), \tilde{u} (black), and \tilde{T} (red); (b) $\frac{\sqrt{u''u''}}{u_\tau}$ (black), $\frac{\sqrt{v''v''}}{u_\tau}$ (red), and $\frac{\sqrt{w''w''}}{u_\tau}$ (green).

extracted at the recycling station, which is identical to the inlet of the principal DNS, located $12\delta_{ref}$ upstream of the corner. The boundary layer profiles at this location are given in figure 3. These may be used to specify or verify the boundary conditions in lower-fidelity simulations, such as LES or RANS, when developing new turbulence models and validating predictions against the present DNS.

As is apparent from figure 4, the skin friction in the DNS follows the trend of the van Driest II prediction in the second half of the domain from $x/\delta_{ref} = 13$ to the outlet, although the values of C_f in the DNS are consistently higher with an offset of $\approx 5\%$ compared to VDII (see figure 4b). The wall in the DNS is isothermal at a temperature of 340K. Since the recovery (or adiabatic wall) temperature is $T_r = T_\infty \left(1 + r \frac{\gamma-1}{2} M_\infty^2\right) = 645\text{K}$ (where r is taken to be 0.89), the present DNS is run with a cold wall ($T_w/T_r \approx 0.5$). The offset in the C_f compared to VDII is likely due to the low value of T_w/T_r in the DNS. Duan et al. [36] performed temporal DNSs of Mach 5 boundary layers with varying wall temperature. For a cold wall with $T_w/T_r = 0.5$, they showed an offset of C_f in their DNS compared to VDII of

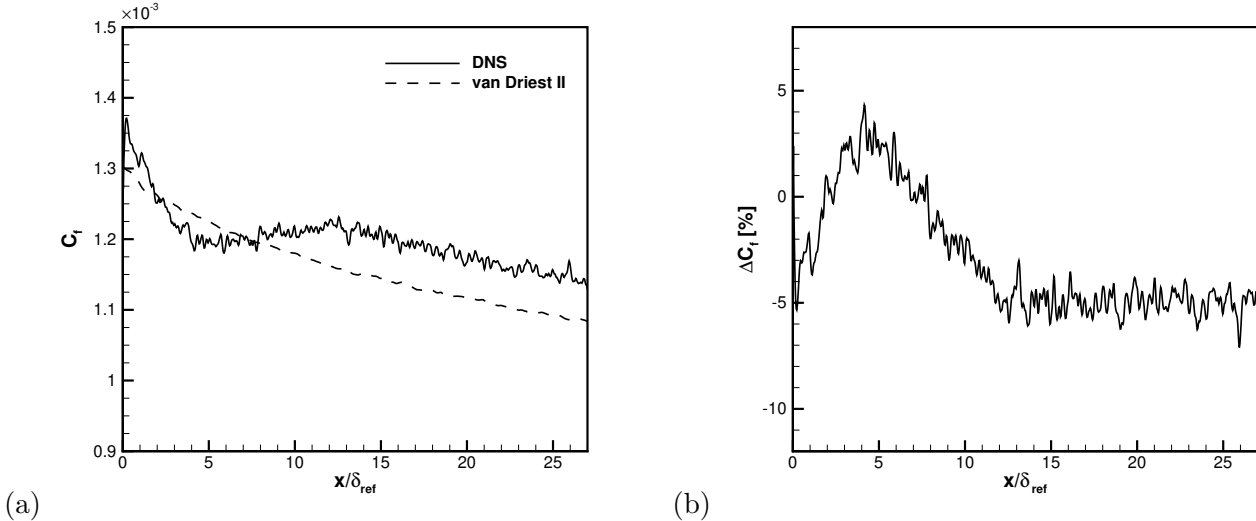


FIG. 4. (a) Time- and spanwise-averaged skin-friction coefficient in the upstream boundary layer (auxiliary DNS) as a function of the streamwise coordinate; (b) relative difference between the van Driest II prediction and the DNS, $\Delta C_f = \frac{C_{f,VDII} - C_{f,DNS}}{C_{f,DNS}}$.

approximately 5%, consistent with the present DNS. It is apparent from figure 4 that in the first half of the domain, from the inlet to $x/\delta_{ref} = 13$, the skin friction does not follow the VDII prediction. This mismatch is due to the transient that the rescaled boundary layer undergoes until it becomes physical at around $x/\delta_{ref} = 13$.

Downstream of $x/\delta_{ref} = 13$, the van Driest transformed velocity profiles, which are shown in figure 5, follow the log law. The presence of the log law indicates that the boundary layer is fully turbulent, although the low Reynolds number causes a small wall-normal extent – at $x/\delta_{ref} = 26.0$, for example, the log law extends from $y^+ = 35$ to 70. Figure 5 shows that the profiles in the present DNS are offset compared to the standard log law $u_{VD}^+ = \frac{1}{\kappa} \ln(y^+) + B$ with $\kappa = 0.41$ and $B = 5.2$. In the present DNS, a value of $B = 5.9$ matches the data. This offset is also likely a wall temperature effect and also consistent with the findings of Duan et al. [36].

Figure 6 shows several spectra at the recycling station. The spectra show a broadband peak around frequencies $O(U_\infty/\delta)$, which are associated with the large-scale, energy-carrying turbulent eddies. Crucially, no spurious energy is present at the frequency characteristic of the rescaling, which is $f_{resc} \approx \frac{U_\infty}{26\delta_{ref}}$. This shows that the rescaling length is chosen large enough to eliminate any artificial correlation due to the rescaling boundary condition.

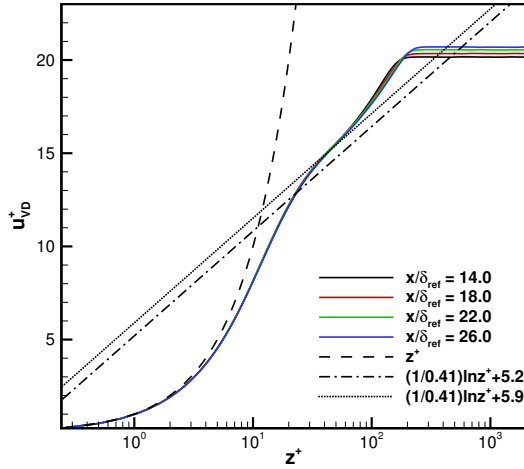


FIG. 5. Van-Driest-transformed velocity profiles in the upstream boundary layer.

The present section has provided an overview of the auxiliary DNS and presented the main results; further details may be found in Priebe & Martín [39].

Compression ramp

Instantaneous and time-averaged flow structure

Figure 7 shows two typical instantaneous visualizations from the DNS. Due to the high Mach number of the flow, combined with a low deflection angle, the shock angle is shallow (inviscid value: 14.3°). As a result, the shock is immersed in the boundary layer in the vicinity of the corner. A distinct shock sheet typically only appears in the freestream, above the turbulent eddies, at a streamwise distance equal to several incoming boundary layer thicknesses downstream of the corner. As is apparent from figure 7, the shock is distorted by the passage of the δ -scale turbulent bulges from the incoming boundary layer. Since these bulges carry lower momentum fluid than the irrotational freestream fluid, the shock relaxes upstream as a bulge travels through it, causing δ -sized ‘ripples’ in the shock sheet. These ripples result in a shock sheet that appears to conform to the boundary layer bulges for up to 10δ downstream of the corner. In figure 7(a), for example, the shock shows the imprint of four δ -sized eddies that have convected through it and that are visible in the boundary layer on the ramp: the first bulge and corresponding imprint on the shock are visible from

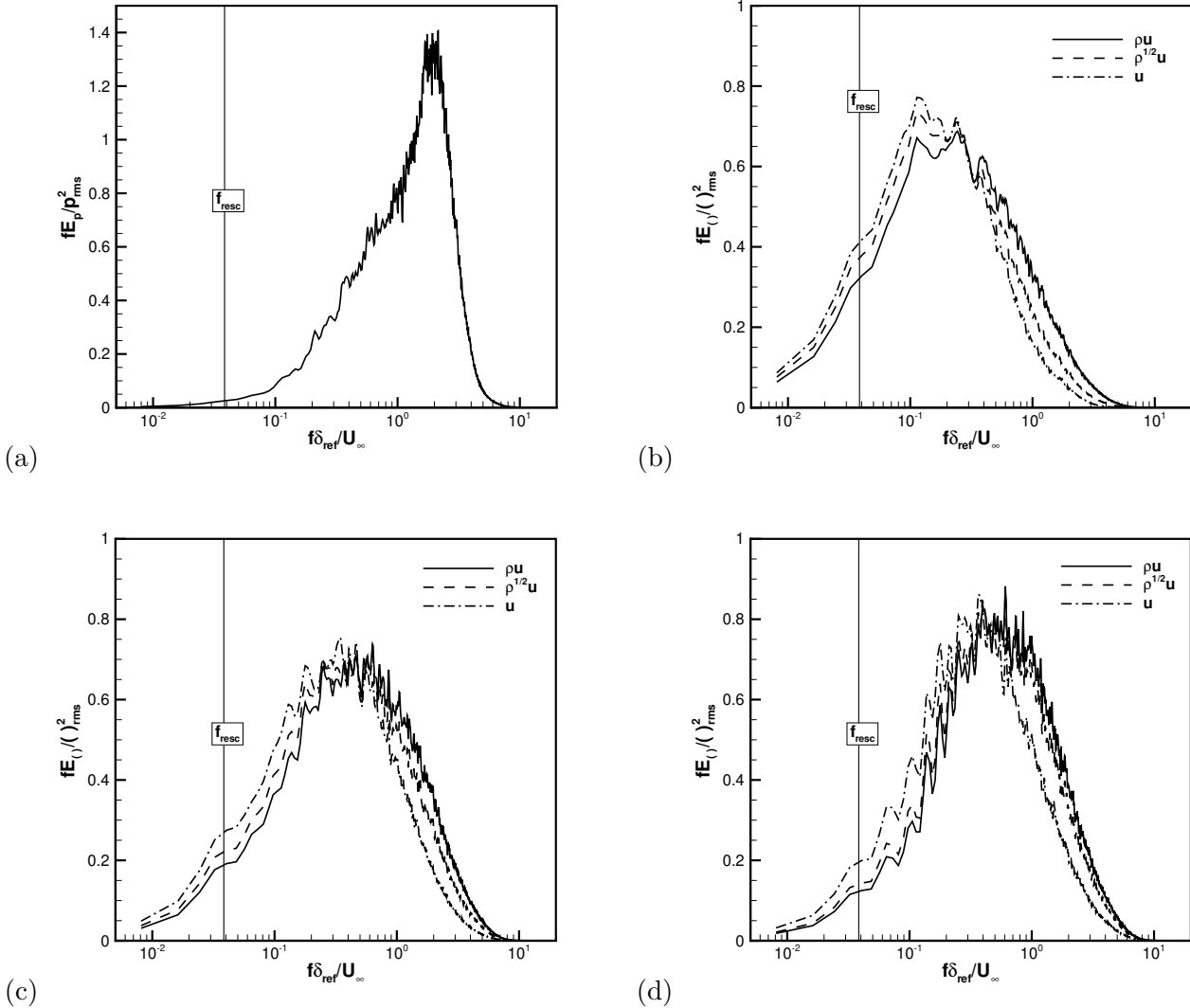


FIG. 6. Spectra in the upstream boundary layer at $x/\delta_{ref} = 26.0$: (a) wall pressure, (b-d) streamwise velocity, momentum, and Morkovin-type scaled velocity at $z^+ = 15$ (b), $z^+ = 50$ (c), and $z/\delta_{ref} = 0.5$ (d). The nominal frequency of the rescaling boundary condition, $f_{resc} = \frac{U_\infty}{26\delta}$, is shown on the spectra.

approximately $x/\delta_{ref} = 13.75$ to 14.5, the second from $x/\delta_{ref} = 14.75$ to 15.75, the third from $x/\delta_{ref} = 16.25$ to 17.25, and the fourth from $x/\delta_{ref} = 18.0$ to 19.0.

Figure 8 shows an instantaneous three-dimensional visualization from the DNS. The three-dimensional nature of the ‘ripples’ in the shock sheet is visible. Since these ripples are caused by the convection of the turbulent bulges from the incoming boundary layer through the shock, the spanwise length scale of the ripples is comparable to that of the

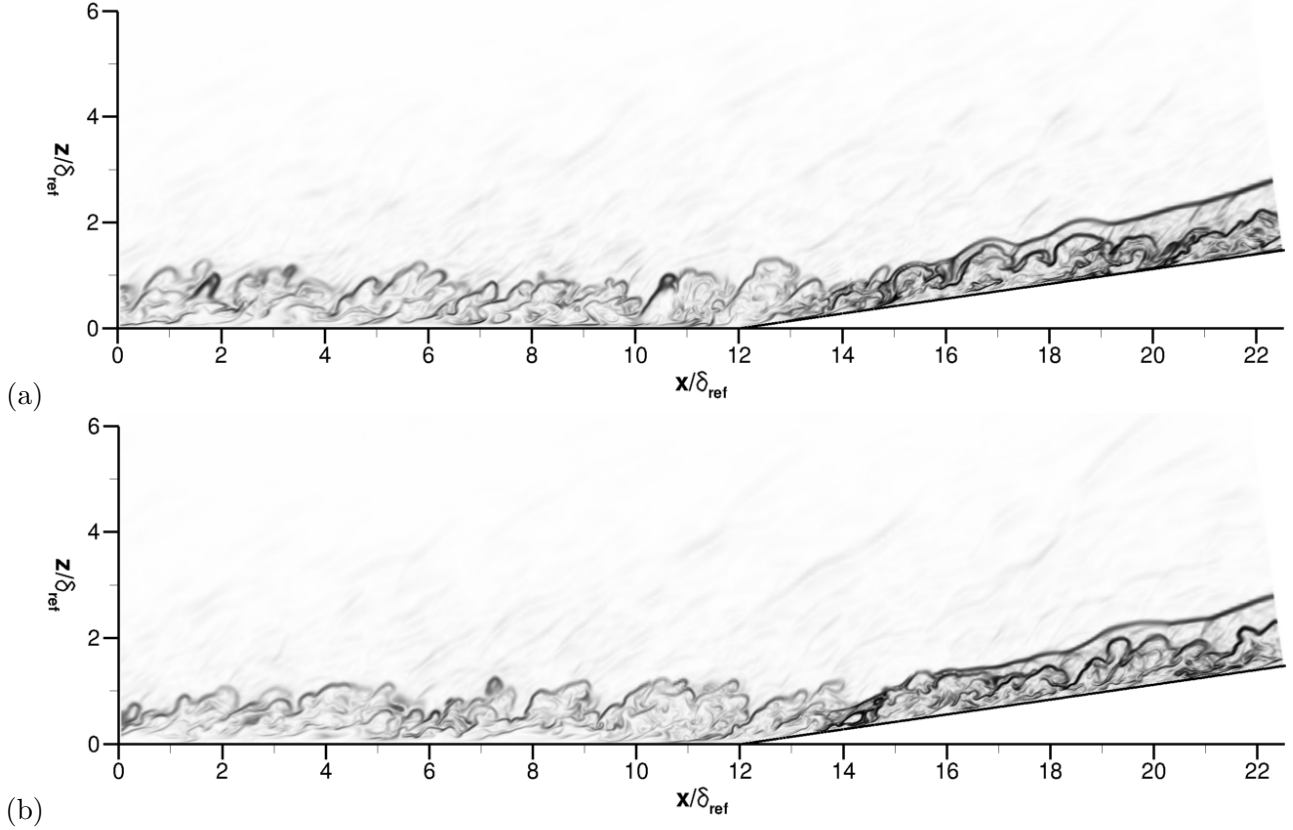


FIG. 7. Numerical Schlieren visualizations of the 8° compression-ramp STBLI (principal DNS).

bulges and thus of $O(\delta)$. It is also apparent that further downstream towards the exit of the computational domain, the imprint of the turbulent bulges on the shock weakens. The intersection of the shock sheet with the exit boundary of the domain is fairly uniform across the span.

The present instantaneous flow structure is in qualitative agreement with the filtered Rayleigh scattering (FRS) visualizations obtained by Bookey et al. [2], see figure 9. The boundary layer bulges appear as dark regions in the FRS images, and the shock is visible as a sharp change from grey in the freestream upstream of the shock to light grey or white downstream. As in the DNS, the shock in the experiment is shallow, immersed in the boundary layer, and once it emerges from the boundary layer it shows the ‘imprint’ of the δ -sized turbulent bulges that have convected through it.

The mean shock structure from DNS is shown in figure 10. It is apparent that in the time-averaged sense the shock is essentially attached at the corner. The shock angle at the exit of the computational domain is approximately 13.5° , which is approaching the inviscid

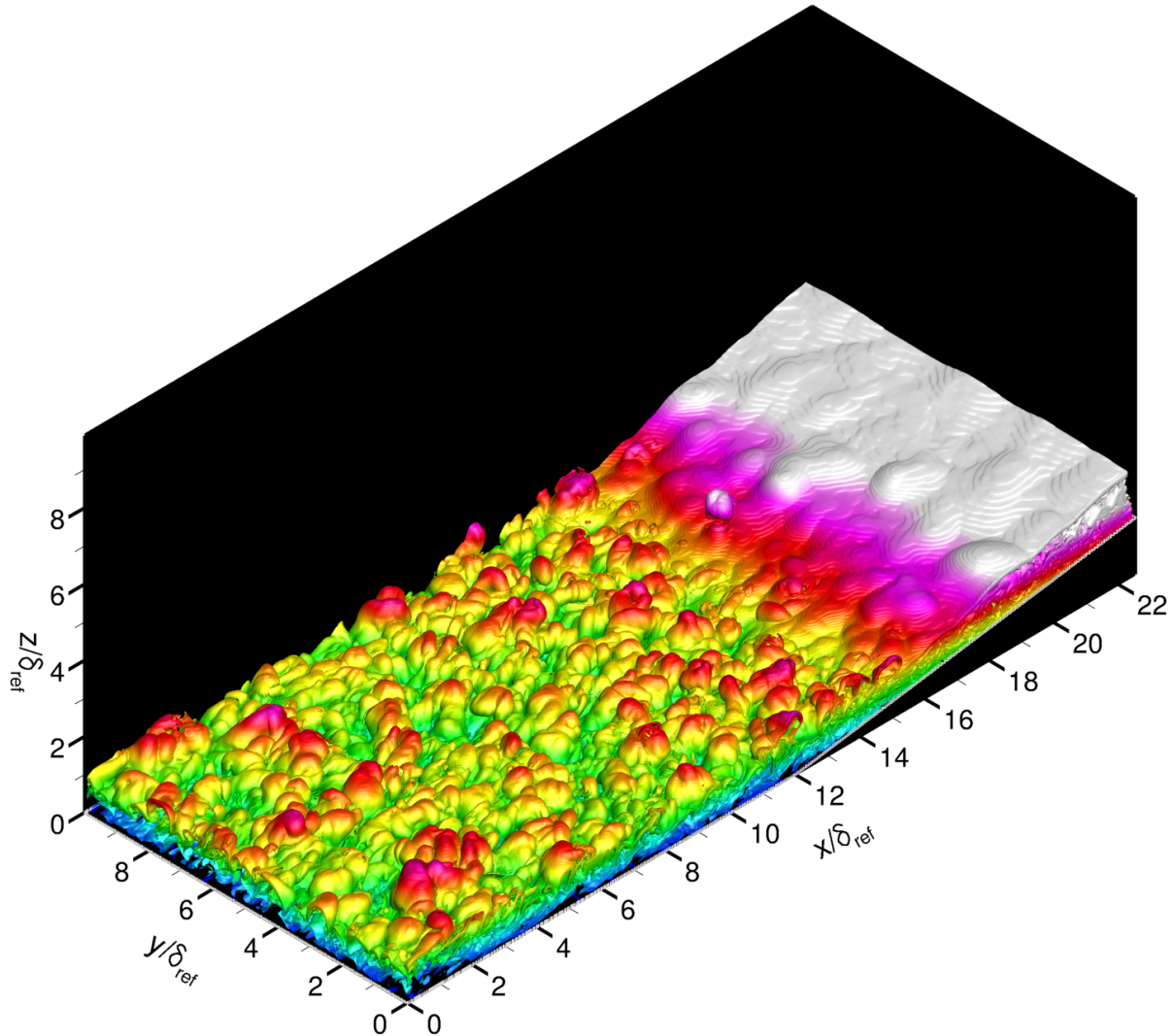


FIG. 8. Instantaneous, three-dimensional flow structure. Isosurface of the magnitude of the density gradient, colored by the wall-normal coordinate.

value of 14.3° . The mean shock structure observed in the DNS is in agreement with the corresponding experimental Schlieren visualizations in Schreyer et al. [4], which also show the time-averaged shock to be attached at the corner.

Surface quantities

The time- and spanwise-averaged wall pressure distribution is shown in figure 11(a). The ratio of the downstream-to-upstream wall pressure is $p_d/p_u \approx 3.45$, which is close to the

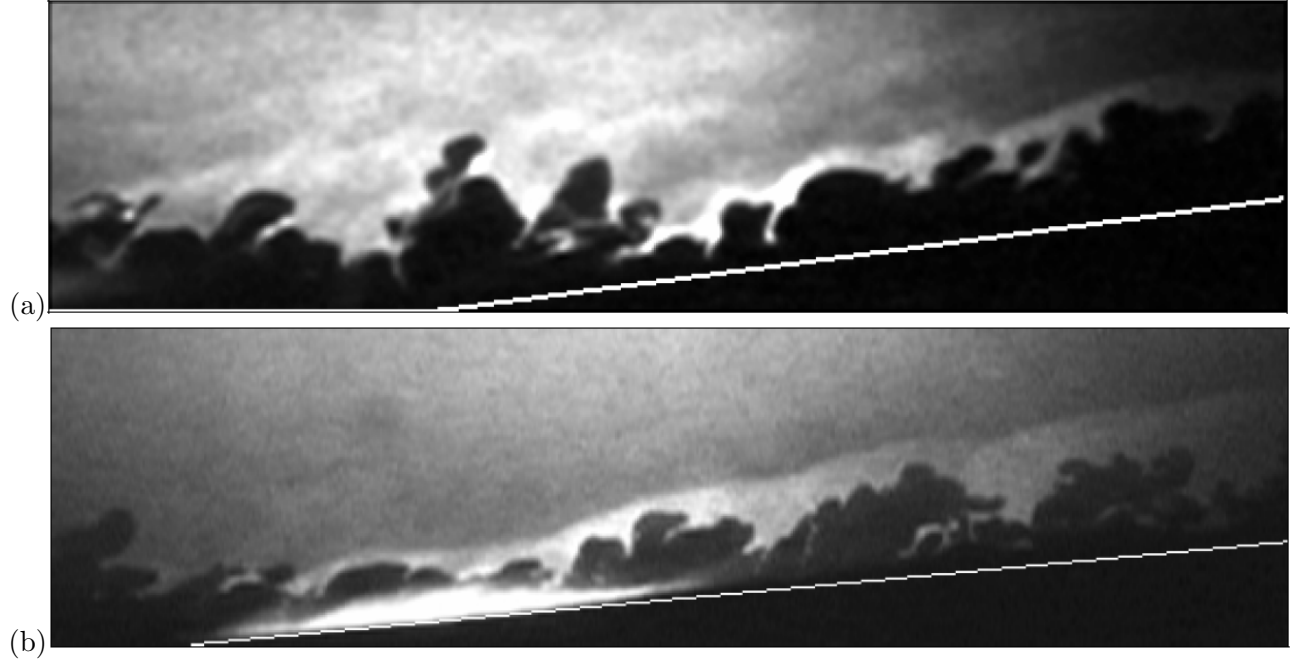


FIG. 9. Filtered Rayleigh scattering images of the 8° compression-ramp interaction. Reproduced from Bookey et al. [2], see also Schreyer et al. [4].

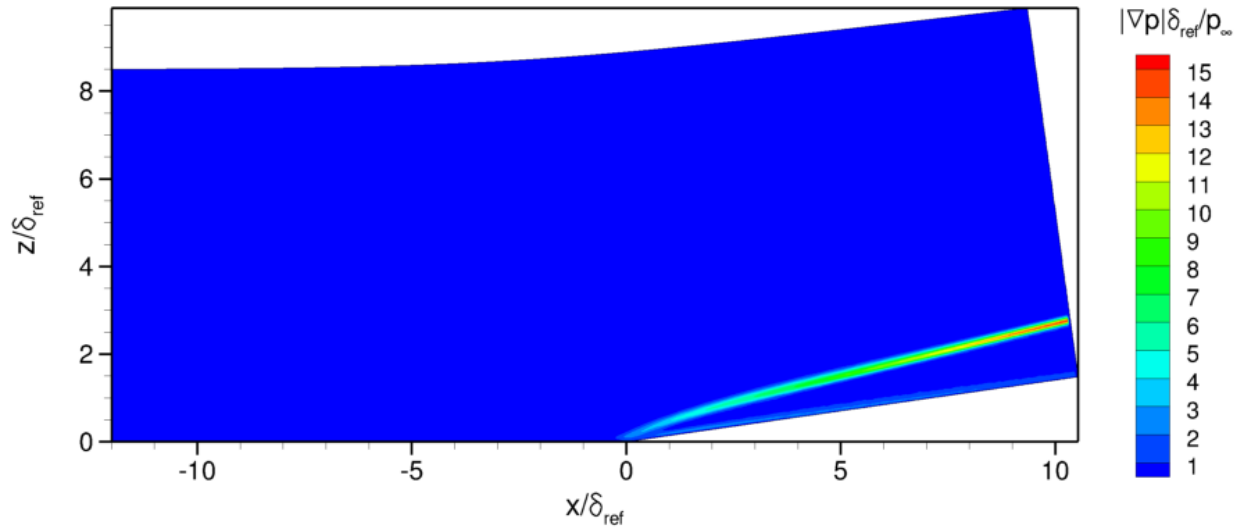


FIG. 10. Time- and spanwise-averaged pressure gradient magnitude.

inviscid value of 3.51. The slightly lower pressure ratio in the DNS compared to the inviscid value is consistent with the observation made from figure 10 that the shock angle is lower than the inviscid value. The present domain extends $10.5\delta_{ref}$ downstream of the corner, and while this is sufficient to give a shock strength close to the inviscid one, an even longer

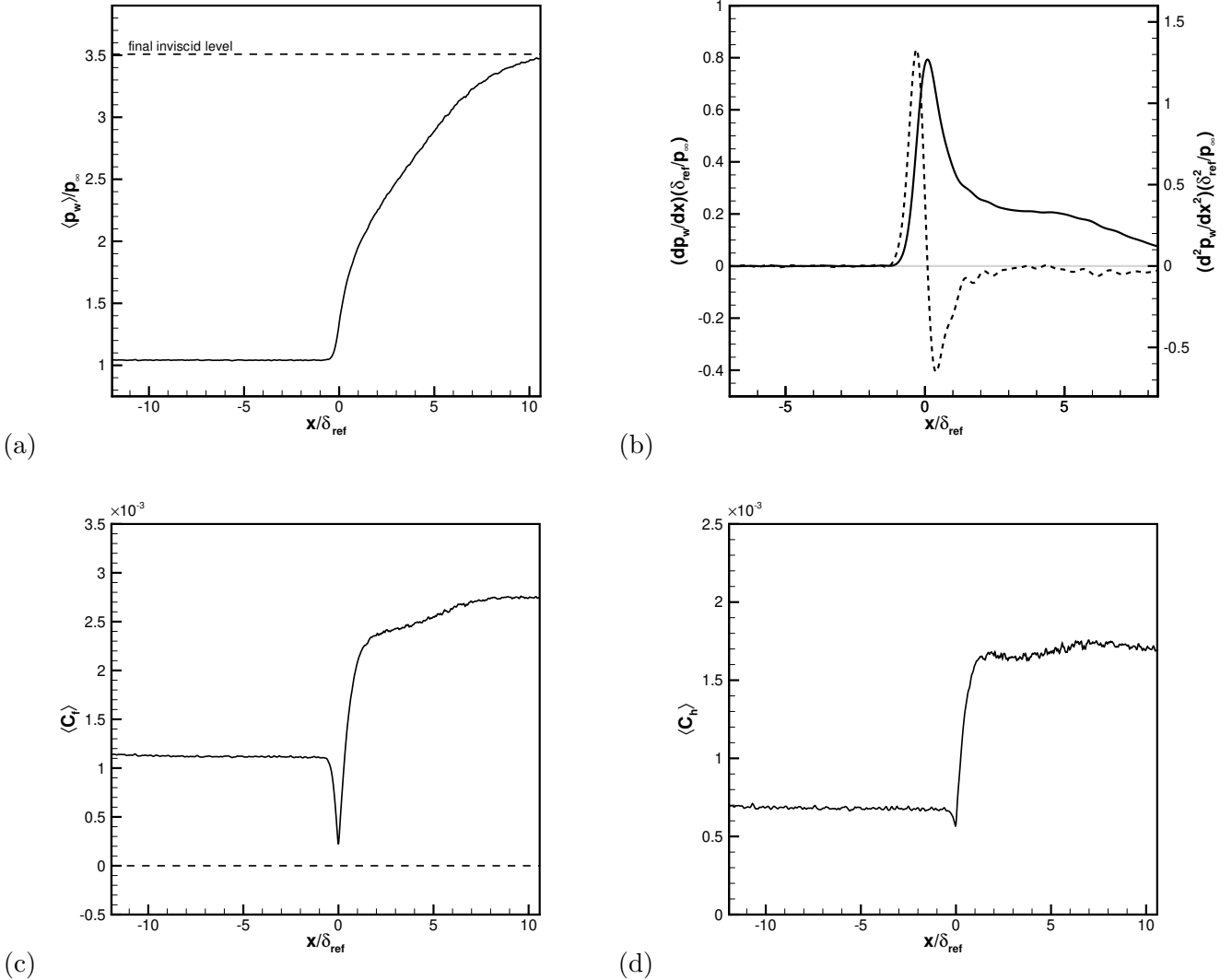


FIG. 11. Time- and spanwise-averaged surface quantities through the interaction: (a) wall pressure, (b) first derivative (solid) and second derivative (dashed) of the wall pressure with respect to the streamwise coordinate x , (c) skin-friction coefficient, and (d) Stanton number.

computational domain would be required to reach the full inviscid strength of the shock, as is often also the case in supersonic interactions (e.g. Wu & Martín [32] and Priebe et al. [34]).

The time- and spanwise-averaged skin friction coefficient C_f is shown in figure 11(c). While the value of C_f decreases significantly upstream of the corner, it does not fall below $C_f = 0$, which indicates that the flow is attached in the mean. Attached flow was also observed in the experiments, as may be seen from the oil flow visualizations in Bookey et

al. [2].

The third surface quantity of interest is the heat transfer coefficient, or Stanton number, which is defined as $C_h = \frac{q_w}{\rho_\infty U_\infty C_p (T_w - T_r)}$, where q_w is the wall heat transfer, T_w is the wall temperature, T_r is the recovery temperature, and ρ_∞ and U_∞ are the density and velocity in the freestream. Figure 11(d) shows the time- and spanwise-averaged C_h distribution. The value of C_h has a minimum at the corner before increasing to a higher level in the downstream flow compared to the upstream flow; the ratio of downstream-to-upstream heat transfer is $C_{h,d}/C_{h,u} = 2.5$.

An interesting feature of the C_f and C_h distributions is the presence of inflection points and local maxima and minima in the downstream flow. C_h , for example, shows local maxima at $x/\delta_{ref} \approx 2$ and 6.5. The resulting ‘scalloped’ shape of the distributions has also been observed by Murray et al. [17] in experiments of an attached axisymmetric reflected STBLI at Mach 9, where it was attributed to the non-equilibrium evolution of the boundary layer as it is subjected to a pressure gradient that changes with streamwise distance. Such a link between the scalloped shape of C_f and C_h and changes in the pressure gradient also appears to exist in the present DNS. As is apparent from figure 11(b), the pressure distribution has an approximately constant slope (and hence zero curvature) between $x/\delta_{ref} \approx 2$ and 6.5, and these locations correspond closely to the peaks of the scalloping in C_f and C_h .

State of separation

As discussed in § , the time- and spanwise-averaged skin-friction coefficient C_f is greater than zero everywhere in the interaction, and the flow is thus attached in the mean. The probability of observing reversed flow on an instantaneous basis is, however, significant. It is apparent from figure 12, which shows a typical contour plot of the instantaneous value of C_f , that the flow is mostly attached in the upstream boundary layer, although small patches of local flow reversal are visible. Near the corner, between approximately $x/\delta_{ref} = 11.5$ and $x/\delta_{ref} = 12.5$, relatively large regions of reversed flow are visible. These regions can extend up to approximately $0.5\delta_{ref}$ in the streamwise and spanwise directions, and they appear to be uniformly distributed across the span of the computational domain. Further downstream, in the out-of-equilibrium boundary layer on the ramp, the size and number of the reversed flow regions appear to gradually decrease with increasing distance from the corner.

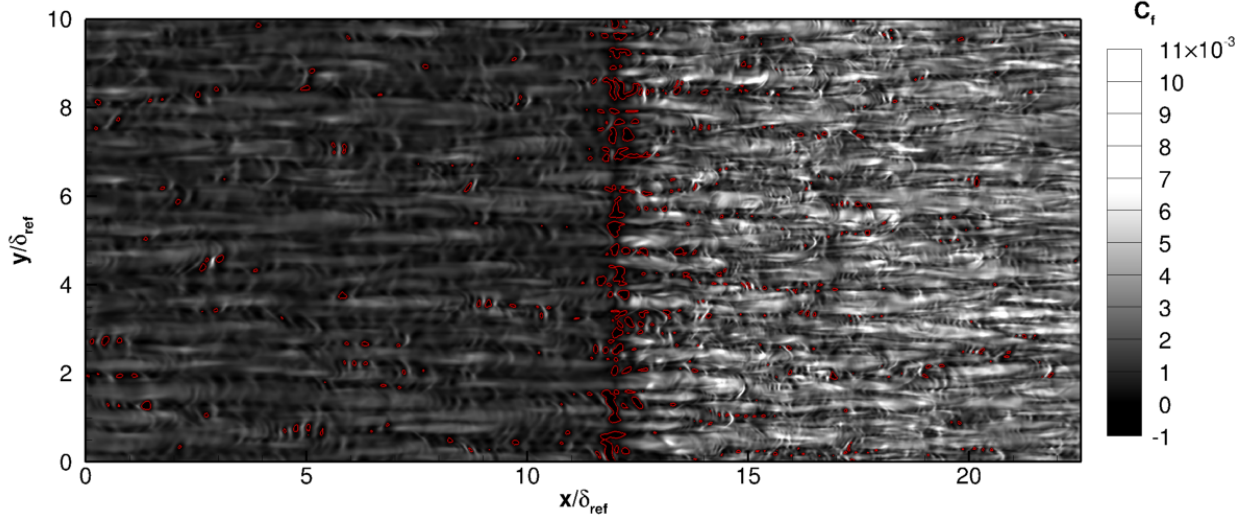


FIG. 12. Instantaneous contours of the skin-friction coefficient C_f . The red line is the $C_f = 0$ contour.

The spanwise-averaged probability $\bar{\gamma}_u$ of flow reversal ($u < 0$) is shown in figure 13 (note that the overbar indicates spanwise-averaging). Following Simpson [40], the state of separation may be classified based on the observed values of γ_u : The flow is said to be in the *incipient detachment (ID)* state when $\gamma_u = 0.01$, i.e. when the flow is reversed 1% of the time; it is said to be in the *intermittent transitory detachment (ITD)* state when $\gamma_u = 0.2$; and in the *transitory detachment (TD)* state when $\gamma_u = 0.5$. It is apparent from figure 13(a) that the flow in the vicinity of the corner is in the ITD state. The values of $\bar{\gamma}_u$ lie above the ITD threshold of 0.2 in a streamwise window of approximately $0.25\delta_{ref}$ surrounding the corner (between approximately $x/\delta_{ref} = 11.85$ and 12.1). The maximum value of $\bar{\gamma}_u$ is observed at the corner and is 0.31. Figure 13(a) also shows that $\bar{\gamma}_u$ crosses the ID threshold from below at approximately $x/\delta_{ref} = 11.5$ (or $0.5\delta_{ref}$ upstream of the corner), and from above at approximately $x/\delta_{ref} = 13.75$ (or $1.75\delta_{ref}$ downstream of the corner). Figure 13(b) shows that the region, in which significant non-zero values of $\bar{\gamma}_u$ are observed, is thin; at its highest point above the wall, the $\bar{\gamma}_u = 0.02$ contour line extends to approximately $(z - z_{wall})/\delta_{ref} = 0.04$. The present analysis of the reversed flow structure and probability in a hypersonic STBLI may be compared to similar analyses in the literature for lower Mach number cases, see Na & Moin [41], who investigated an incompressible separation bubble using DNS, and Pirozzoli et al. [42], who investigated an incipiently separated transonic

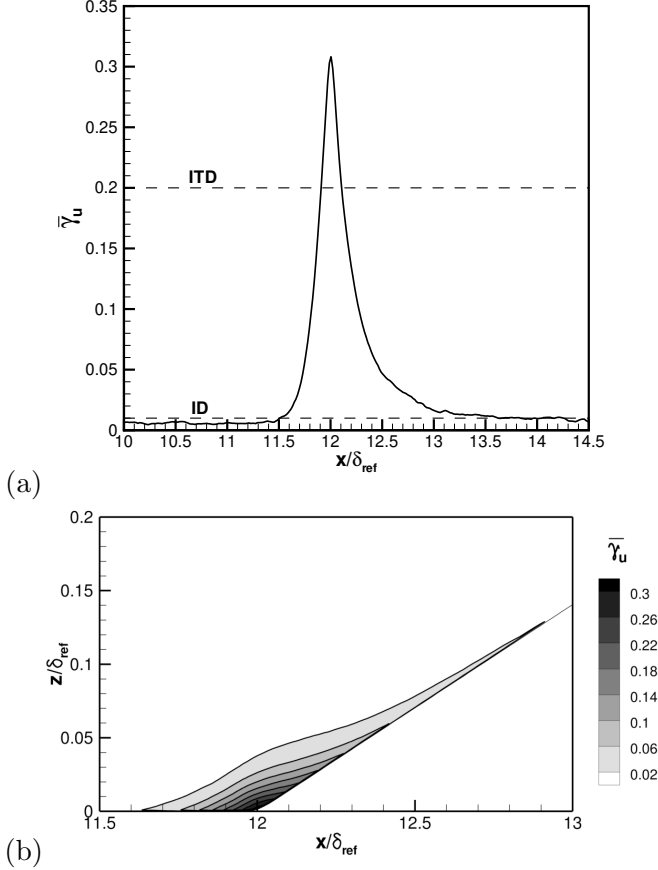


FIG. 13. Spanwise-averaged probability $\bar{\gamma}_u$ of flow reversal: (a) at the first grid point above the wall, and (b) in the streamwise–wall normal plane.

STBLI using DNS.

While figure 13 shows the spanwise-averaged probability of flow reversal, figure 14 shows the three-dimensional probability. The isosurface corresponding to the ID threshold $\gamma_{u,\Delta T} = 0.01$ is shown in figure 14(a), and the isosurface corresponding to the ITD threshold $\gamma_{u,\Delta T} = 0.2$ is shown in figure 14(b). Despite the significant time duration of the present DNS of $\Delta T = 94.4\delta/U_\infty$, the isosurfaces shown in figure 14 are not fully converged. Following the nomenclature used in Na & Moin [41], the dependence of the flow reversal probability on the particular averaging time chosen is emphasized by the subscript ΔT . It is apparent from figure 14 that both the ID and ITD isosurfaces show some variation in the spanwise direction. The structure of the ID isosurface may be described as streaky, and the ITD isosurface is made up of distinct patches that are distributed across the span of the domain.

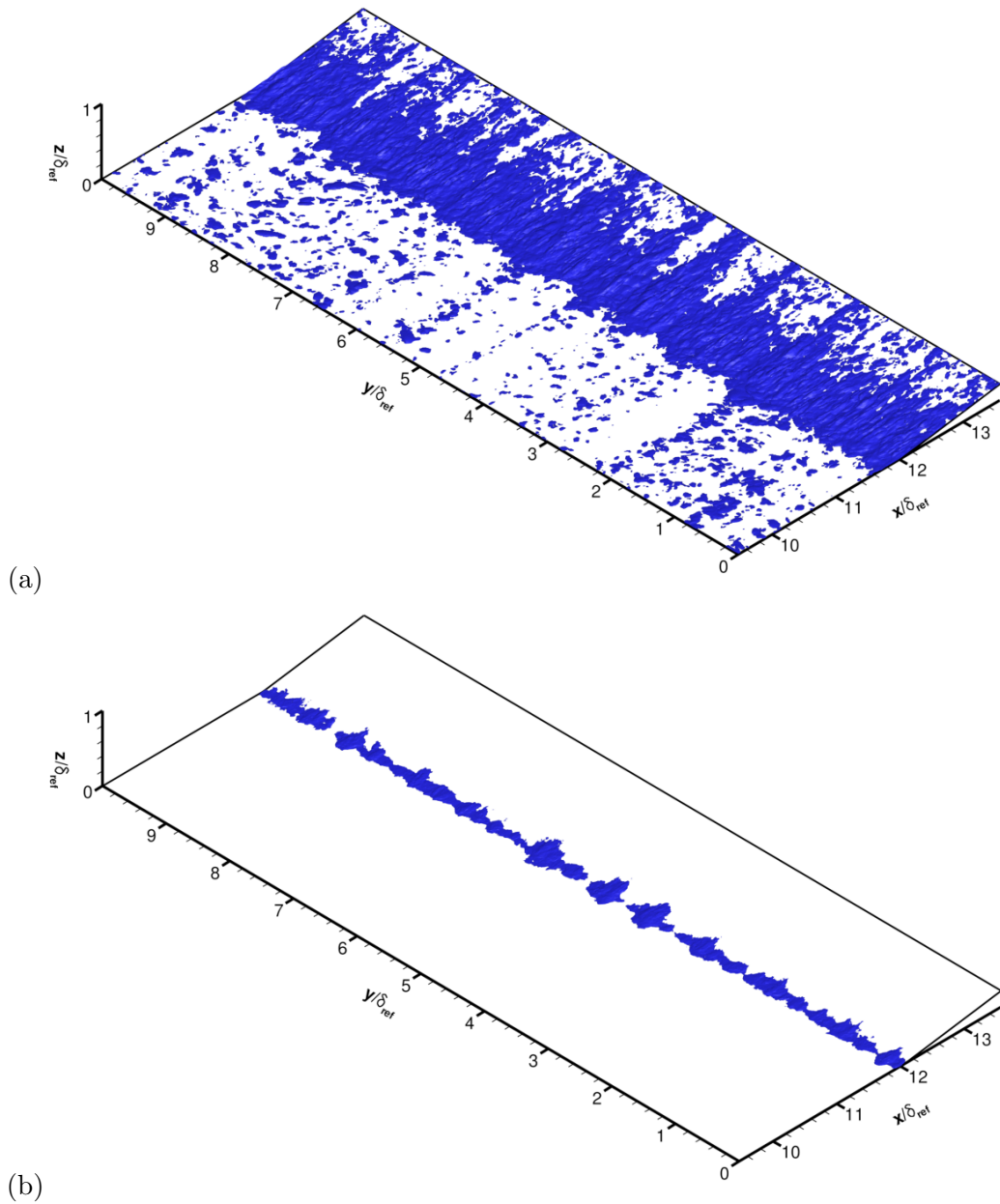


FIG. 14. Probability of flow reversal: (a) isosurface $\gamma_{u,\Delta T} = 0.01$, and (b) isosurface $\gamma_{u,\Delta T} = 0.2$.

Note that while the three-dimensional probability in figure 14 is not fully converged, the other statistics shown in this paper, including the flow reversal probability in figure 13, are spanwise-averaged and have been verified to be converged by comparing statistics for the full DNS to those for half the time duration.

Mean flow field

Figure 15 shows the mean profiles of u -velocity, w -velocity, density, and temperature at six streamwise locations. The profiles have been extracted along the wall normal, and the streamwise coordinate given for the profiles on the ramp is the coordinate at the ramp wall. While not separated in the mean, the near-wall flow is significantly decelerated as the corner is approached. The \tilde{u} profiles at three streamwise locations (upstream of, at, and downstream of the corner) are shown in figure 16 to highlight the changes in the profiles through the interaction. There is a significant near-wall deficit of \tilde{u} at the corner and the profile has an inflection point as typically seen in adverse pressure gradient flows. Note that in the present flow the inflection point is located close to the wall, at $(z - z_w)/\delta_{ref} = 0.045$, consistent with the fact that the region where a significant probability of reversed flow is observed is also low. Downstream of the corner, the profiles quickly recover as shown by the profile at $x/\delta_{ref} = 1$ in figure 16, which does not have an inflection point. The mean wall-normal velocity \tilde{w} is essentially zero in the upstream boundary layer (figure 15a) and jumps to a positive value downstream of the shock (figures 15c-f) due to the deflection of the flow. The jump in $\bar{\rho}$ and \tilde{T} across the shock is also visible, occurring at an increasing wall-normal distance as x is increased, corresponding to the average shock position: for example, the jump is visible at $z/\delta_{ref} \approx 0.8$ at $x/\delta_{ref} = 2.0$, and $z/\delta_{ref} \approx 1.8$ at $x/\delta_{ref} = 6.0$. The increase in $\bar{\rho}$ is more pronounced than the one in \tilde{T} consistent with inviscid theory, according to which $\frac{\rho_2}{\rho_1} = 2.32$ and $\frac{T_2}{T_1} = 1.51$.

The velocity components shown in figures 15 and 16 are in the (x, y, z) coordinate system, which is aligned with the upstream wall. Downstream of the corner, the ramp-aligned (x_r, y, z_r) coordinate system (rotated by 8°) may be used. Figure 17 shows a comparison of the mean velocity components in both coordinate systems at several streamwise locations downstream of the corner. Since the ramp angle is shallow at 8° , \tilde{u} and \tilde{u}_r are essentially identical. As expected, the \tilde{w} and \tilde{w}_r profiles are shifted (in the freestream, the shift is $-U_\infty \sin(8^\circ)$) but the shape of the profiles is similar. There are, however, some differences: for example, \tilde{w} shows a near-wall maximum at $(z - z_w)/\delta_{ref} \approx 0.05$, while \tilde{w}_r does not. In what follows, the mean and fluctuating velocity components are usually taken in the ramp-aligned coordinate system when plotting quantities downstream of the corner. One exception are the Reynolds stress contours for the entire domain, which will be shown in

figure 18. These are based on the upstream coordinate system to avoid the discontinuity at the corner that would result from a change in the coordinate system there. It has been verified that the differences between quantities in the two coordinate systems are generally small, consistent with the low ramp angle of 8° .

Turbulence behavior through the interaction

Figure 18 shows contours of the Favre-averaged Reynolds stresses; the normal stresses $\widetilde{u''u''}$, $\widetilde{v''v''}$, $\widetilde{w''w''}$, and the shear stress $\widetilde{u''w''}$ are shown. It is apparent that the Reynolds stresses are amplified in the interaction region, which may be quantified by considering the amplification tensor $A_{i,j} = \frac{\max_d(\widetilde{u''_i u''_j})}{\max_u(\widetilde{u''_i u''_j})}$ ($i, j = 1, 2, 3$), i.e. the ratio of the maximum value of a particular component of the Reynolds stress in the downstream flow to the maximum value in the upstream flow. The observed values of A are $A_{11} = 1.82$, $A_{22} = 2.53$, $A_{33} = 2.28$, and $A_{13} = 2.12$, i.e. the strongest amplification is in the spanwise component, followed by the wall-normal component, and the weakest amplification is in the streamwise component. The PIV measurements of Schreyer et al. [4] also show that the streamwise fluctuations are amplified less than the wall-normal fluctuations.

The shock causes a decrease in u and an increase in w . Consequently, it is associated with a negative shear stress (see figure 18d). As typically observed in supersonic STBLIs (e.g. Piponnaiu et al. [43]), the shock is associated with a strong peak in $\widetilde{w''w''}$. The reason for this is that the average w , which is close to zero in the upstream boundary layer (there is only a small positive component due to the displacement effect of the boundary layer), jumps to a large positive value across the shock due to the deflection of the flow. As a result, any difference between the instantaneous and the average shock position leads to a relatively strong fluctuation w'' , which explains the peak in $\widetilde{w''w''}$.

Figure 19 shows contours of the TKE $\frac{\widetilde{u''_i u''_i}}{2}$ through the interaction. It is apparent that the locus of points where the maximum values of TKE occur in the boundary layer coincides with a mean streamline (streamline 2 in figure 19, which coincides with the wall-normal location of the inner fluctuation peak in the upstream boundary layer). This may be compared with the behavior typically seen in separated supersonic interactions, where a detached shear layer is formed. In the flow downstream of the shock, the peak Reynolds stresses and TKE values are then found farther away from the wall. Note that in the present attached

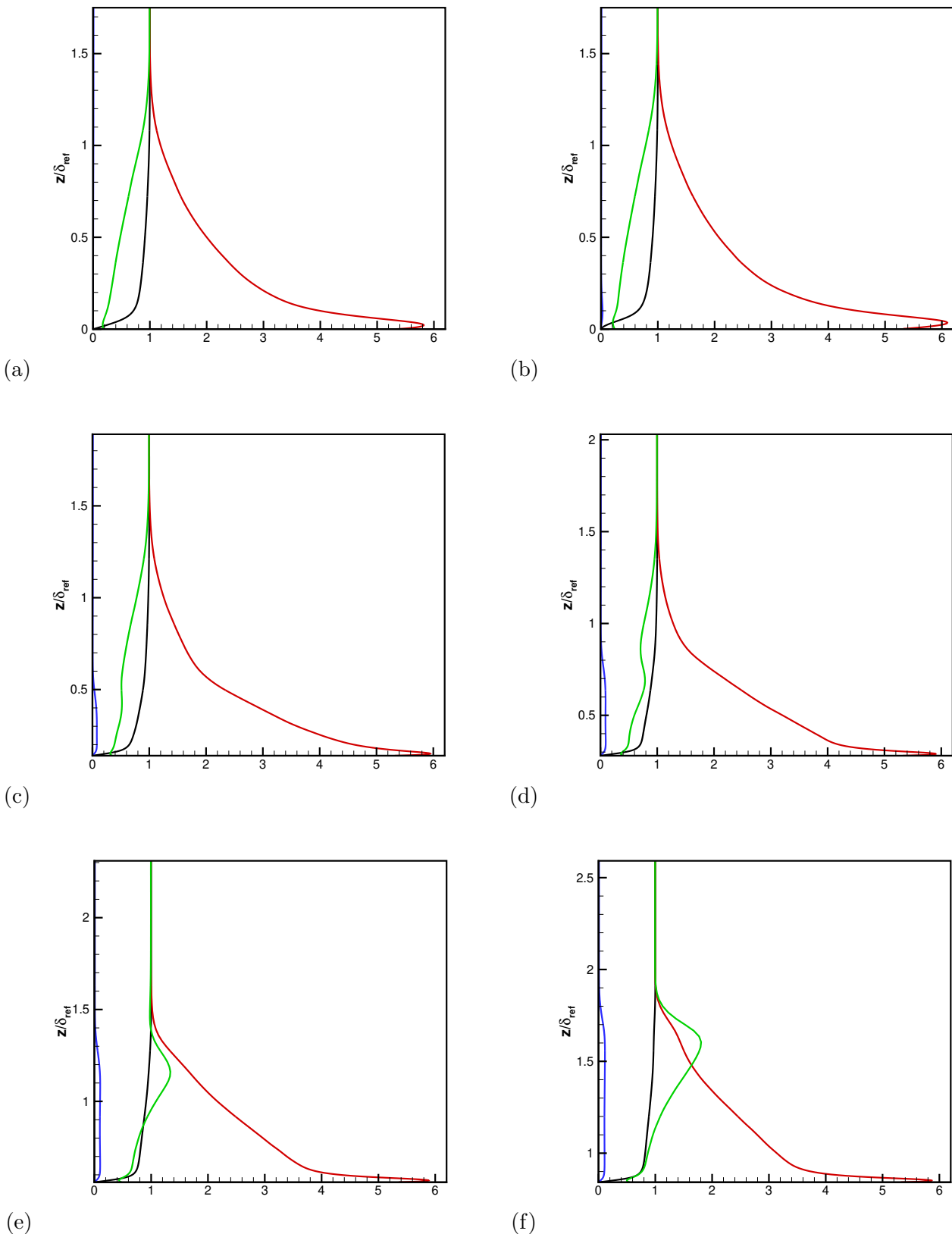


FIG. 15. Profiles of $\bar{\rho}$ (green), \tilde{u} (black), \tilde{w} (blue), and \tilde{T} (red) through the interaction: (a) $x/\delta = -4.0$, (b) $x/\delta = 0.0$, (c) $x/\delta = 1.0$, (d) $x/\delta = 2.0$, (e) $x/\delta = 4.0$, and (f) $x/\delta = 6.0$.

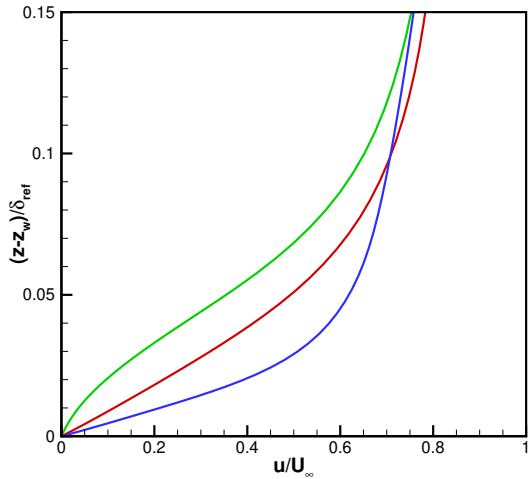


FIG. 16. Near-wall detail of profiles of streamwise velocity \tilde{u} at $x/\delta_{ref} = -4$ (red), $x/\delta_{ref} = 0$ (green), and $x/\delta_{ref} = 1$ (blue).

flow, the structure of the Reynolds stresses and TKE does change somewhat as we move downstream. The contour lines of e.g. $\widetilde{u''u''}$ and TKE bulge towards higher wall-normal locations z between $x/\delta \approx 0 - 5$, which indicates a broadening of the fluctuation peak and is consistent with increased activity away from the wall as is typically seen in adverse pressure gradient flows. This is also apparent from the Reynolds stress profiles in figure 20. The profiles of the streamwise component, for example, show a slight broadening of the fluctuation peak including increased fluctuations away from the wall. However, the wall-normal location of the fluctuation peak remains close to the wall. At the corner, the peak is located only very slightly farther away from the wall than in the incoming boundary layer. Note that the fluctuation peak is probably expected to remain close to the wall since the low-speed region at the corner is thin and the inflection point in the velocity profiles is located close to the wall.

The Reynolds stress anisotropy tensor b_{ij} is defined as: $b_{ij} = \frac{\widetilde{u''_i u''_j}}{2k} - \frac{\delta_{ij}}{3}$ where $k = \frac{\widetilde{u''_i u''_i}}{2}$ is the turbulent kinetic energy and δ_{ij} is the Kronecker function. The second and third invariants of the anisotropy tensor are: $II = -\frac{b_{ij}b_{ji}}{2}$, and $III = \frac{b_{ij}b_{jk}b_{ki}}{3}$ (the first invariant, which is the trace, is zero). As shown by Lumley & Newman [44], and Choi & Lumley [45], realizability imposes constraints on the possible values of II and III. In the $(-II, III)$ -plane, the realizability region is enclosed in a ‘triangular’ boundary, referred to as the Lumley

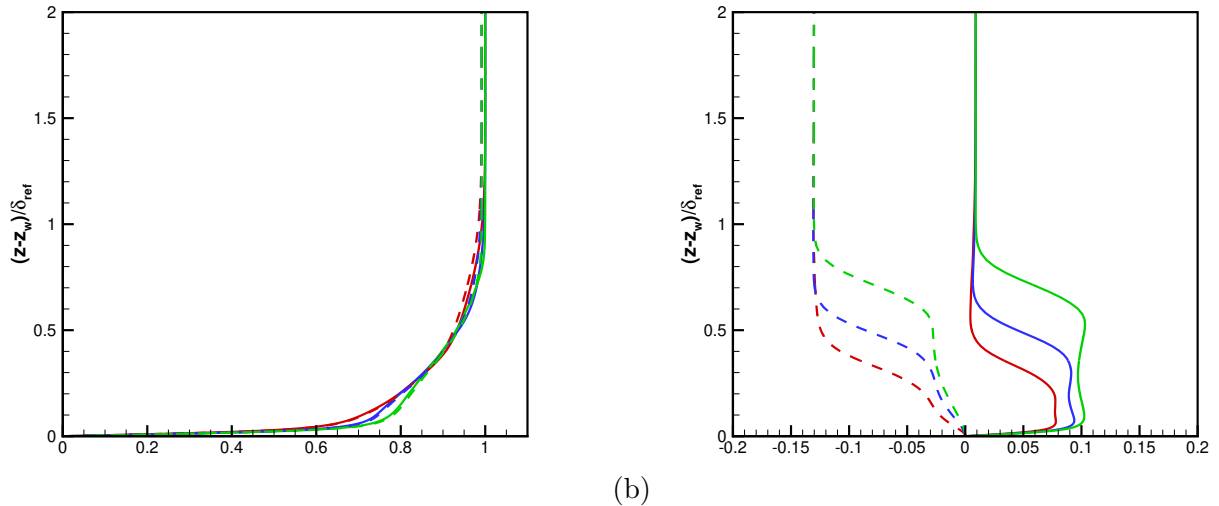


FIG. 17. Comparison of the mean velocity profiles in the (x, y, z) coordinate system aligned with the upstream wall and the (x_r, y, z_r) coordinate system aligned with the ramp: (a) \tilde{u} (solid) vs. \tilde{u}_r (dashed), and (b) \tilde{w} (solid) vs. \tilde{w}_r (dashed). The streamwise locations shown are: $x/\delta_{ref} = 1$ (red), $x/\delta_{ref} = 2$ (blue), and $x/\delta_{ref} = 4$ (green).

triangle.

Figure 21(a) shows the Lumley triangle and the trace of the invariant pair $(-II, III)$ as a function of the wall-normal coordinate z in the undisturbed boundary layer of the present DNS. Near the wall ($z^+ < 8$), the invariants follow the top boundary of the Lumley triangle, which corresponds to two-component turbulence. In this near-wall region, the normal fluctuations w'' are damped by the presence of the wall. Since the streamwise component becomes more dominant as z is increased, the invariant pair moves towards the top right corner of the Lumley triangle, which corresponds to one-component turbulence. As z is increased further, the invariant pair moves along the bottom right boundary of the Lumley triangle, which corresponds to axisymmetric turbulence with one of the components (in this case, u'') being larger than the other two. At the edge of the boundary layer ($z/\delta = 1$), the invariant pair is close to the bottom corner of the Lumley triangle, which corresponds to an isotropic Reynolds stress tensor. The trace of the invariant pair is typical for attached shear layers. A qualitatively identical behavior is shown in Pope [46], figure 11.1, for incompressible channel flow, and in Pirozzoli et al. [42] and Grilli et al. [47] for supersonic boundary layers.

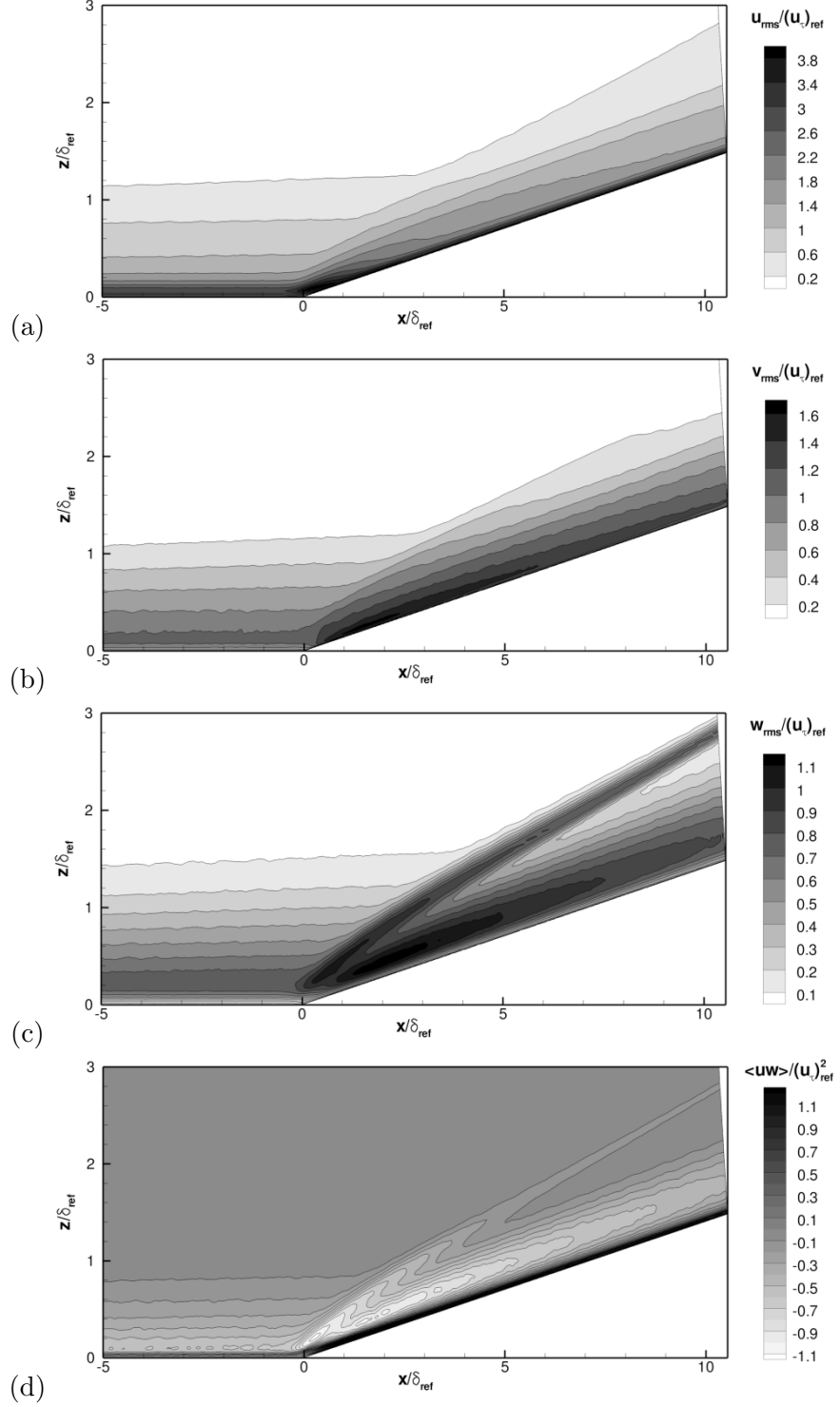


FIG. 18. Time- and spanwise-averaged contours of the (a) streamwise velocity fluctuation intensity $\sqrt{u''u''}/u_{\tau,\text{ref}}$, (b) spanwise velocity fluctuation intensity $\sqrt{v''v''}/u_{\tau,\text{ref}}$, (c) wall-normal velocity fluctuation intensity $\sqrt{w''w''}/u_{\tau,\text{ref}}$, and (d) Reynolds shear stress $\langle uw \rangle / (u_{\tau,\text{ref}})^2$. The normalization is by the upstream friction velocity obtained at the recycling station of the auxiliary DNS, which is equivalent to the inlet of the principal DNS.

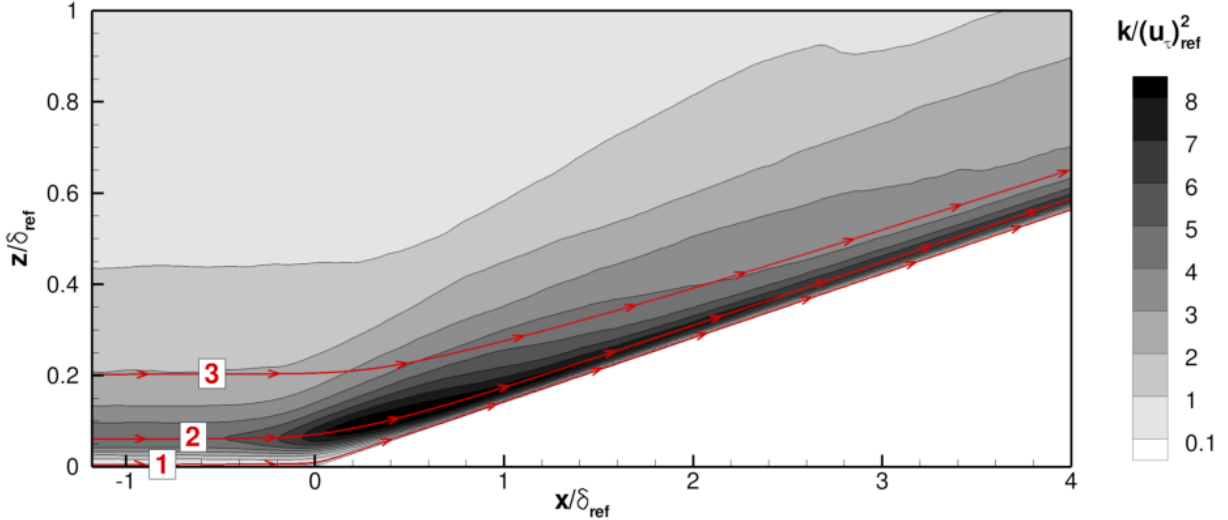


FIG. 19. Time- and spanwise-averaged field of the Favre-averaged turbulent kinetic energy. The three streamlines used in figure 23 are also shown.

As is apparent from figures 21 and 22, the anisotropy of the Reynolds stress tensor changes through the interaction. The evolution of the invariant pair along three streamlines is shown in figure 23: the first streamline is located close to the wall (it passes through $z^+ = 1$ at $x/\delta = -4.0$), the second is located at the inner-peak location in the upstream boundary layer (it passes through $z^+ = 12$ at $x/\delta = -4.0$), and the third is located in the log layer in the upstream boundary layer (it passes through $z/\delta = 0.2$ at $x/\delta = -4.0$). It is apparent from figure 23 that the invariant pair $(-II, III)$ traces a ‘U’-shape as the streamwise coordinate is increased through the interaction. The anisotropy first moves towards the origin of the Lumley triangle, before then relaxing away from it again. The movement towards the origin occurs because both $-II$ and III decrease as the turbulence is subjected to the adverse pressure gradient and becomes more isotropic. This behavior is also visible by looking at the Lumley triangles at several locations through the interaction (figures 21 and 22): it is apparent, especially in figures 22(b-d), that the invariant trace is pulled towards the origin of the Lumley triangle. The main physics shown in these plots is thus the effect of the shock and adverse pressure gradient on the anisotropy of the velocity fluctuations, which become more isotropic in the interaction. Lumley triangles for an incipiently separated transonic STBLI (Pirozzoli et al. [42]) and a separated supersonic STBLI (Grilli et al. [47]) have also previously shown that the fluctuations become more isotropic in the near-wall region in the

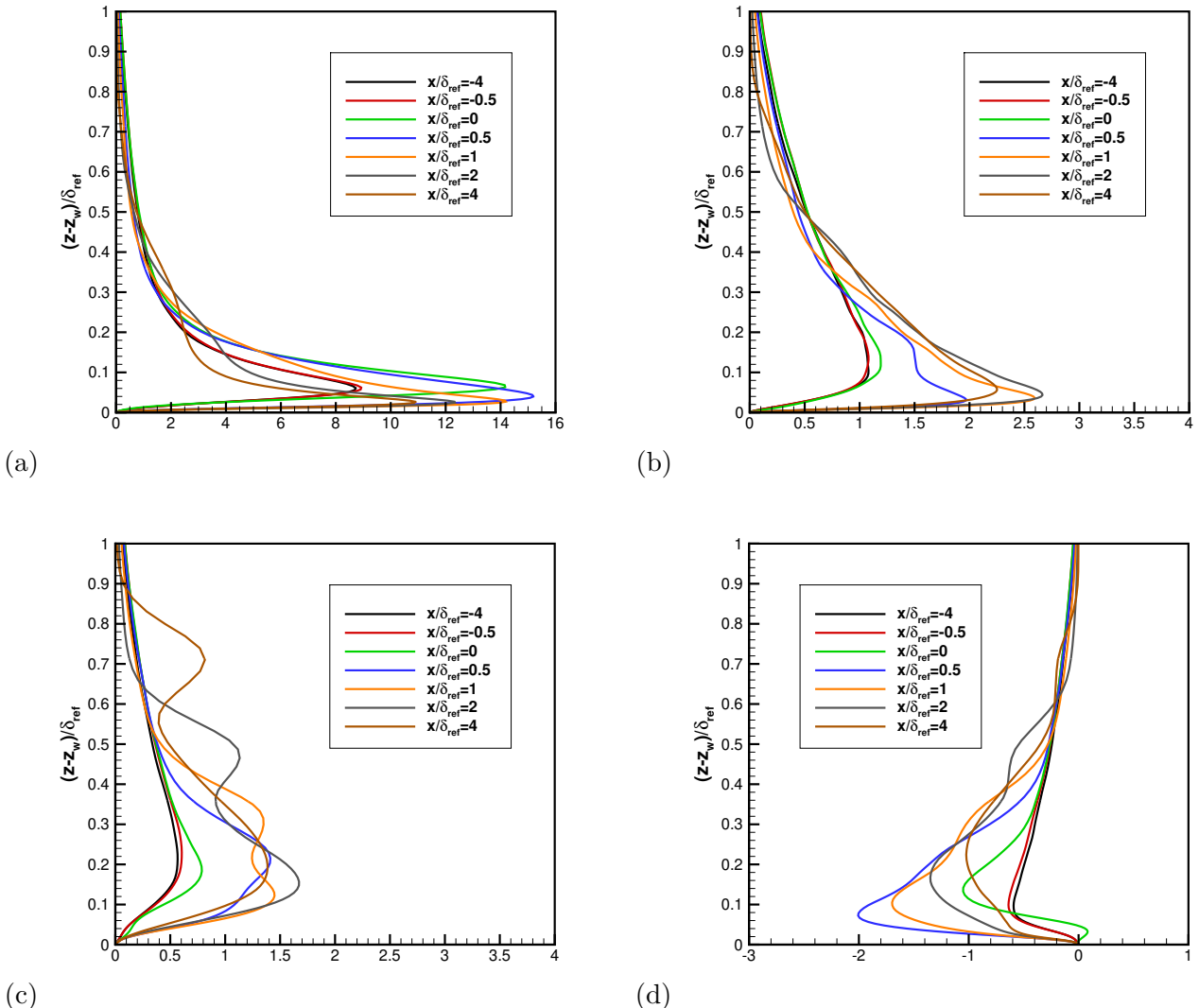


FIG. 20. Reynolds stress profiles at several locations through the interaction: (a) $\widetilde{u_r'' u_r''}/u_{\tau,ref}^2$, (b) $\widetilde{v_r'' v_r''}/u_{\tau,ref}^2$, (c) $\widetilde{w_r'' w_r''}/u_{\tau,ref}^2$, and (d) $\widetilde{u_r'' w_r''}/u_{\tau,ref}^2$.

interaction.

Figure 24 shows the wall pressure spectra in the upstream boundary layer and at several locations around the corner and on the ramp. The signals were sampled at a frequency of approximately $f_s \delta/U_\infty = 126$. A single broadband peak is maintained at all locations, but with the following changes: (1) The rms of the wall pressure fluctuations increases, which is shown by the increase in the area under the (premultiplied and non-normalized) spectra. At $x/\delta = 5.0$, for example, $p_{w,rms}/p_\infty = 0.51$ compared to 0.13 in the upstream boundary layer. (2) The central frequency of the broadband peak shifts to lower values

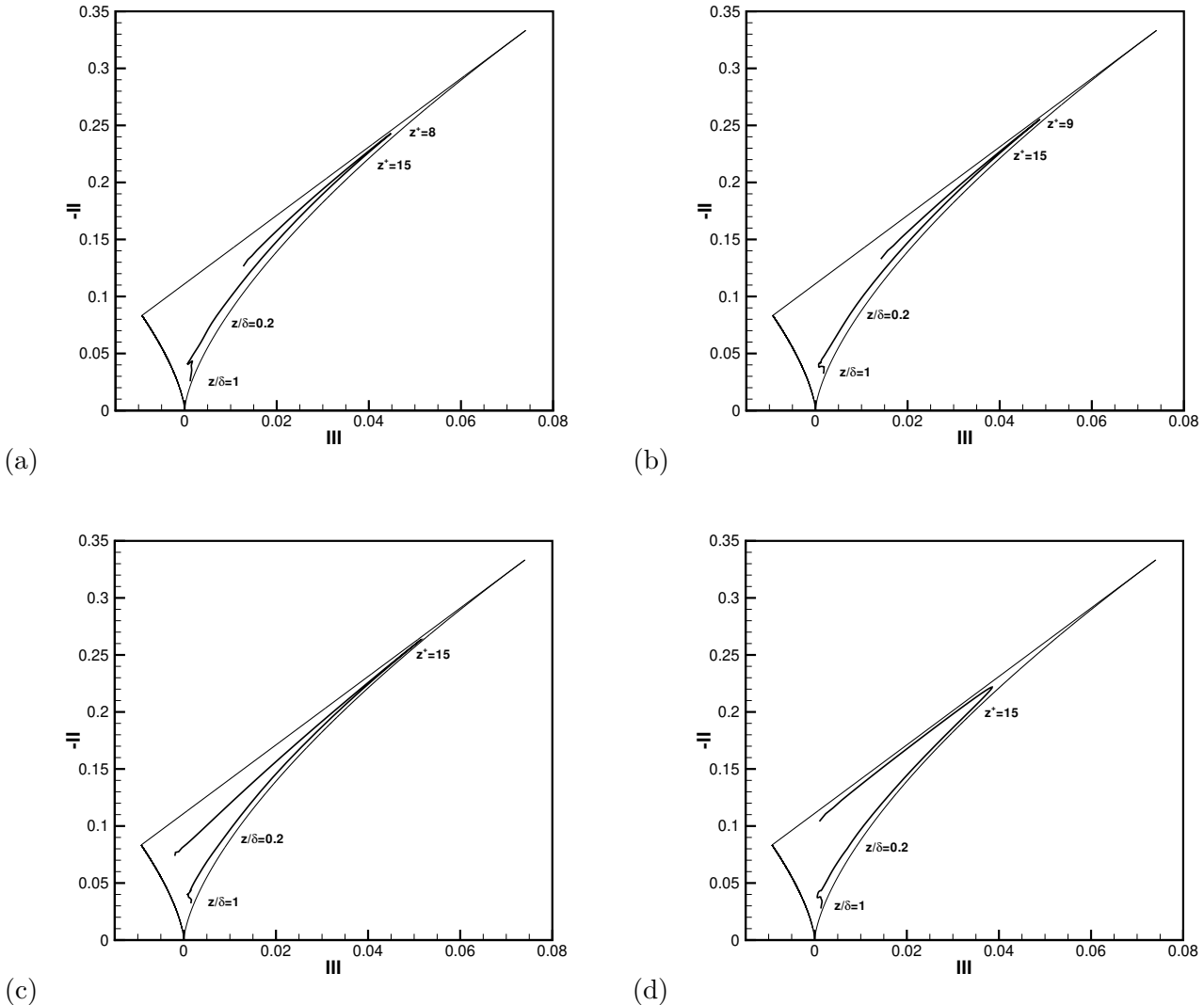


FIG. 21. Lumley triangles. Each subfigure shows the trace of the invariant pair $(-II, III)$ of the Reynolds stress anisotropy tensor as a function of the wall-normal coordinate, z , for a fixed streamwise location, x : (a) $x/\delta = -4.0$, (b) $x/\delta = -0.25$, (c) $x/\delta = 0.0$, and (d) $x/\delta = 0.5$.

downstream of the shock compared to the upstream boundary layer. At $x/\delta = 5.0$, it is $f\delta/U_\infty \approx 0.9$ compared to $f\delta/U_\infty \approx 2.0$ in the upstream boundary layer. The spectra are resolved down to a low frequency of $f\delta_{ref}/U_\infty \approx 0.02$, and while they show an increase in low-frequency energy (at, say, $f\delta_{ref}/U_\infty < 0.1$) downstream of the shock compared to the upstream boundary layer, there is no distinct spectral peak at low frequencies in this attached interaction. The absence of significant low-frequency unsteadiness is consistent with observations in supersonic STBLIs. Strong supersonic interactions with mean flow sep-

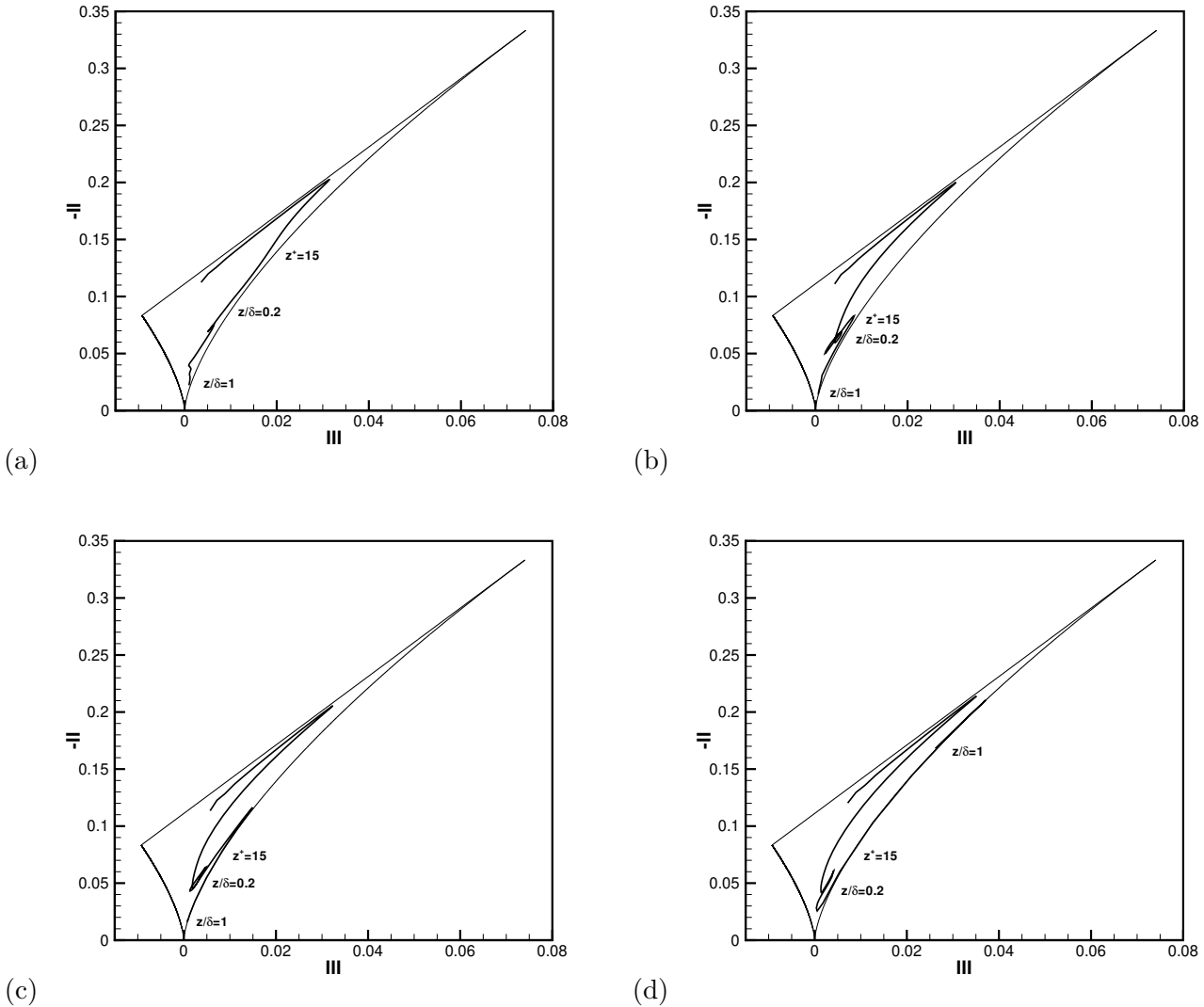


FIG. 22. Lumley triangles as in figure 21 but at the streamwise locations: (a) $x/\delta = 1.0$, (b) $x/\delta = 2.0$, (c) $x/\delta = 3.0$, and (d) $x/\delta = 5.0$.

aration show an energetic, broadband, low-frequency unsteadiness with a central frequency typically in the range $St_L = fL_{sep}/U_\infty = 0.02 - 0.05$, where L_{sep} is the separation length (e.g. Dussauge et al. [48], Clemens & Narayanaswamy [49]). However, weaker cases, including incipiently separated ones, do not show such a distinct and energetic low-frequency spectral peak (Piponnau et al. [43]).

The TKE budget in the undisturbed upstream boundary layer ($x/\delta = -4$) is given in figure 25(a). Note that the TKE budget terms are defined here as in Wilcox [50], p. 247. As typically seen in attached boundary layers (see e.g. Duan et al. [36, 37]), viscous diffusion

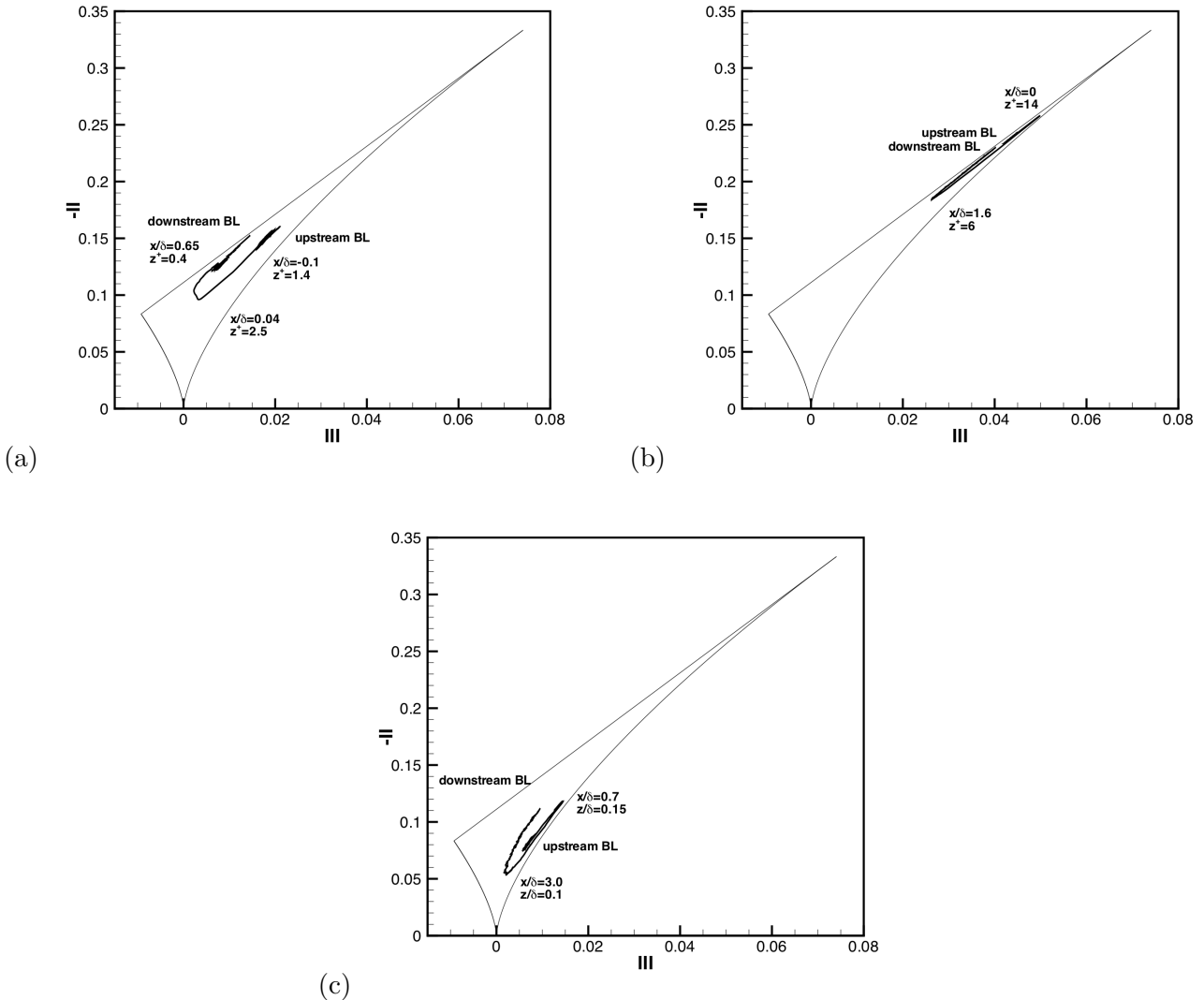


FIG. 23. Traces of the invariant pair $(-II, III)$ of the Reynolds stress anisotropy tensor along three mean-flow streamlines: (a) along the streamline passing through $z^+ = 1$ at $x/\delta = -4$, (b) along the streamline passing through $z^+ = 12$ at $x/\delta = -4$, and (c) along the streamline passing through $z/\delta = 0.2$ at $x/\delta = -4$. See also figure 19 for the location of the streamlines.

and dissipation are the dominant terms in the viscous sublayer, where they balance (with smaller contributions coming from pressure diffusion and dilatation). The production peak is at $z^+ \approx 15$ and is balanced by viscous dissipation, turbulent transport and viscous diffusion. In the log layer and outer part of the boundary layer, production and dissipation balance. As the corner is approached, the magnitude of the peak production increases significantly (see figure 25b,c at $x/\delta = -0.25, 0$). The additional production is balanced primarily by an

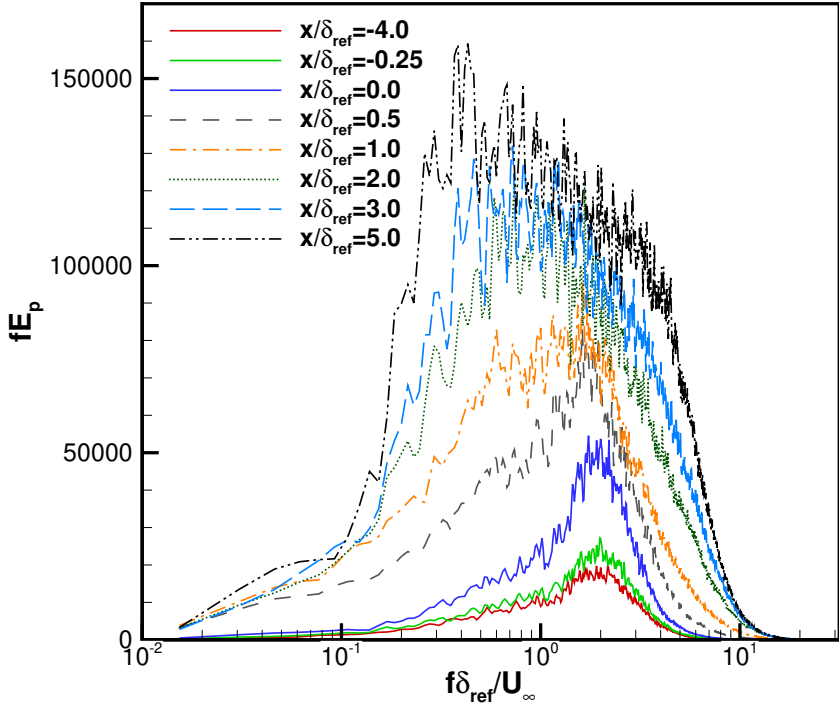


FIG. 24. Premultiplied spectra of wall pressure fluctuations
at several streamwise locations.

additional convection term contribution that is present near the corner. Further downstream at $x/\delta = 0.5$ and 1 (figure 25(d) and 26(a)), significant contributions of the pressure diffusion term, the convection term, and the turbulent transport are seen in the region $z^+ = 20 - 100$. At the farthest locations downstream ($x/\delta = 3$ and 5, see figure 26(c,d)), the inner part of the boundary layer recovers to an equilibrium state with the balances mentioned in the description of figure 25(a) at work.

While figure 26(b-d) focuses on the near-wall region, figure 27 shows one of the profiles, at $x/\delta = 5.0$, on a larger wall-normal scale. The region between $z^+ = 130$ and 220, where significant variations in the TKE budget terms occur, is associated with the shock. The behavior in this region is due to the unsteadiness of the shock, which smooths the shock jump in the mean, generates a local fluctuation peak (e.g. figure 18), and leads to the budget terms shown in figure 27.

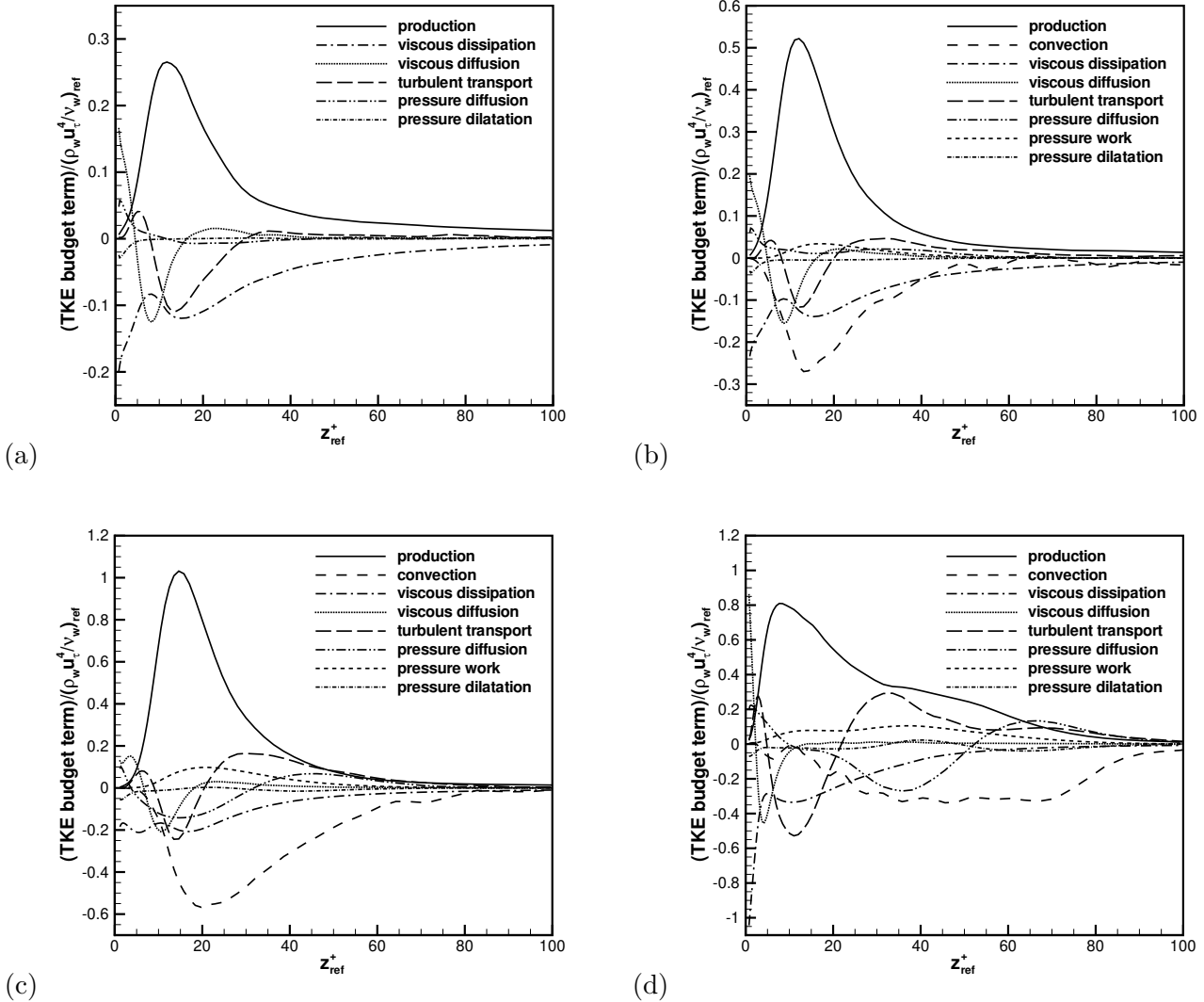


FIG. 25. TKE budget at various streamwise locations: (a) $x/\delta = -4.0$, (b) $x/\delta = -0.25$, (c) $x/\delta = 0.0$, and (d) $x/\delta = 0.5$.

Surface heat flux and the turbulent temperature field

Standard RANS models typically do not predict hypersonic STBLIs accurately. The prediction of the surface heat flux is particularly difficult as discussed in the introduction. For example, Roy & Blottner [20] conclude that ‘while some of the turbulence models do provide reasonable predictions for the surface pressure, the predictions for surface heat flux are generally poor, and often in error by a factor of four or more’.

We have verified several scalings linking the velocity field to the temperature field. The

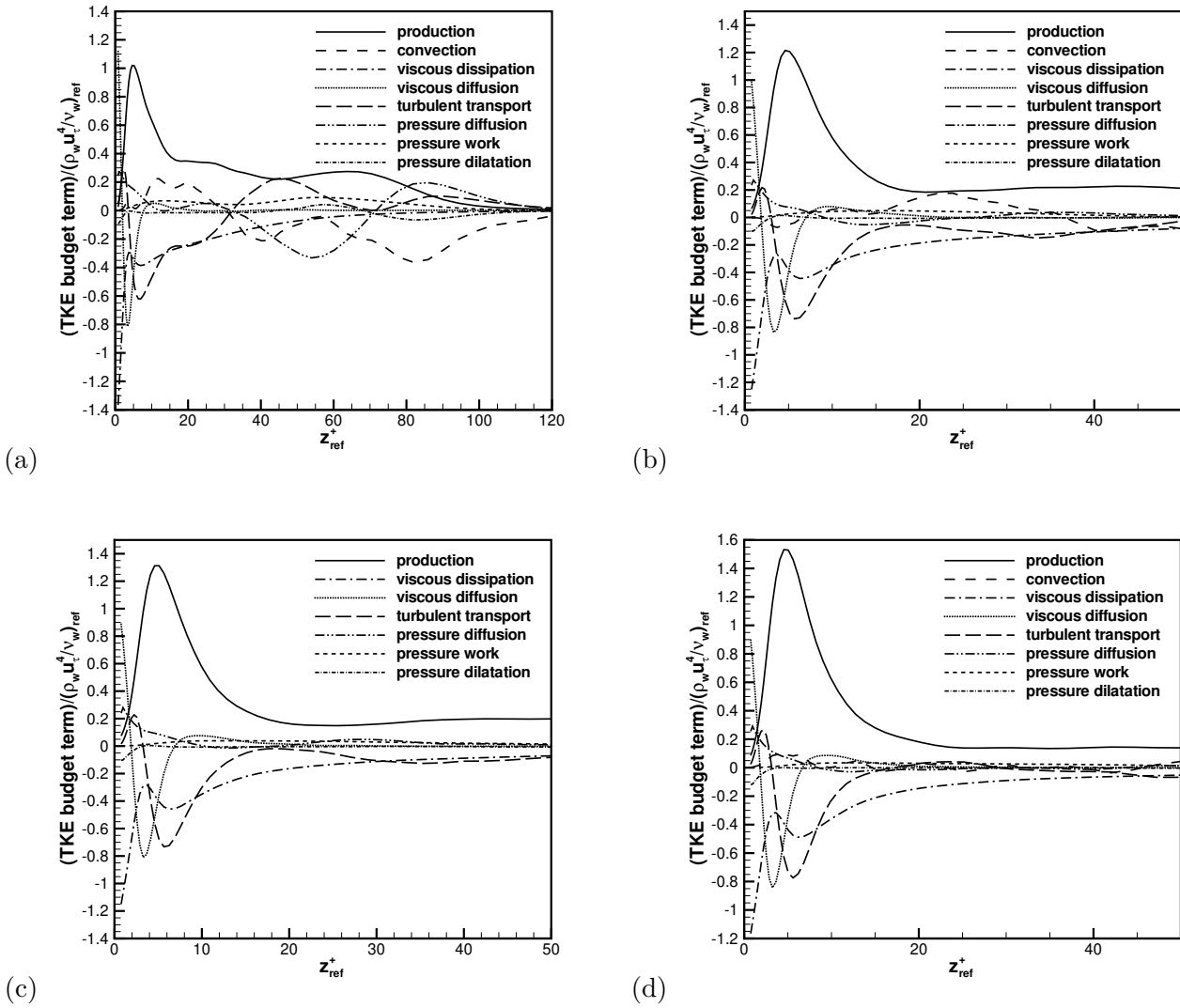


FIG. 26. TKE budget at various streamwise locations: (a) $x/\delta = 1.0$, (b) $x/\delta = 2.0$, (c) $x/\delta = 3.0$, and (d) $x/\delta = 5.0$.

simplest is probably the Reynolds Analogy (RA), which links the mean skin friction coefficient, C_f , to the mean Stanton number, C_h : $RAF = \frac{2C_h}{C_f} = const. \approx 1$. Figure 28(a) shows the Reynolds Analogy factor, RAF , as a function of the streamwise coordinate, x , through the interaction. The Reynolds Analogy is satisfied in the undisturbed upstream boundary layer, where $RAF \approx 1.2$, which is within the range $0.9 < RAF < 1.3$ typically observed in hypersonic zero-pressure-gradient boundary layers (Roy & Blottner [20]). The most significant departures from this range occur around the corner, between $x/\delta = -0.5$ and $x/\delta = 2$, where $RAF \gg 1$. The Reynolds Analogy factor peaks at the corner, where

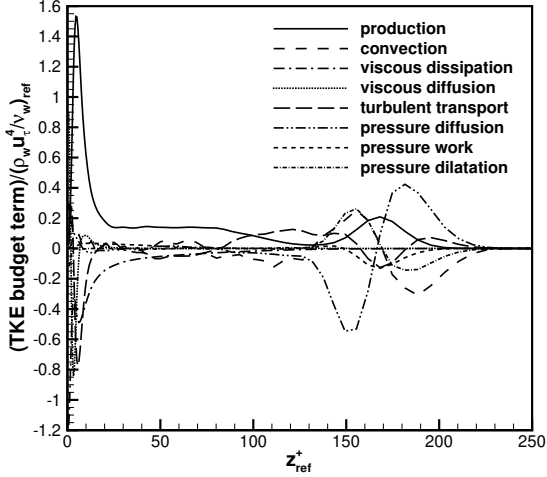


FIG. 27. TKE budget at $x/\delta = 5.0$ and on a larger wall-normal scale than in figure 26(d) to show the shock region.

$RAF = 5.2$. As is apparent from figure 11, this is due to the fact that the skin friction coefficient approaches zero at the corner since the flow is close to separation, whereas the heat transfer coefficient does not. The value of RAF remains above the typical range for zero-pressure-gradient boundary layers for a significant distance downstream of the corner – it is $RAF = 1.53$ at $x/\delta = 1.0$, 1.41 at $x/\delta = 2.0$, 1.34 at $x/\delta = 4.0$ – before dropping to $RAF < 1.3$ downstream of $x/\delta = 5.75$.

Disagreement with the Reynolds Analogy in hypersonic STBLI has previously been observed in the literature, especially for separated cases. The heat transfer tends to scale better with the wall pressure, rather than the skin friction, in these cases (Back & Cuffel [18], Coleman & Stollery [8], Holden [12], Schülein [16], Murray et al. [17]). As shown in figure 28b, the present DNS results show reasonable agreement with the QP85 scaling (Back & Cuffel [18]): $QP85 = \frac{q(x)}{q_u} \left(\frac{p_u}{p(x)} \right)^{0.85} \approx const. \approx 1$, where the subscript ‘u’ denotes upstream values. This scaling has previously been shown to match experiments of hypersonic STBLI (e.g. Holden [12], Murray et al. [17]). As is apparent from figure 28b, there are some departures from the scaling in the regions of strongest adverse pressure gradient in the vicinity of the corner, where the minimum value of $QP85$ is 0.65 and the maximum value is 1.35, but the general agreement is good and the singularity at the corner is reduced compared to the Reynolds Analogy.

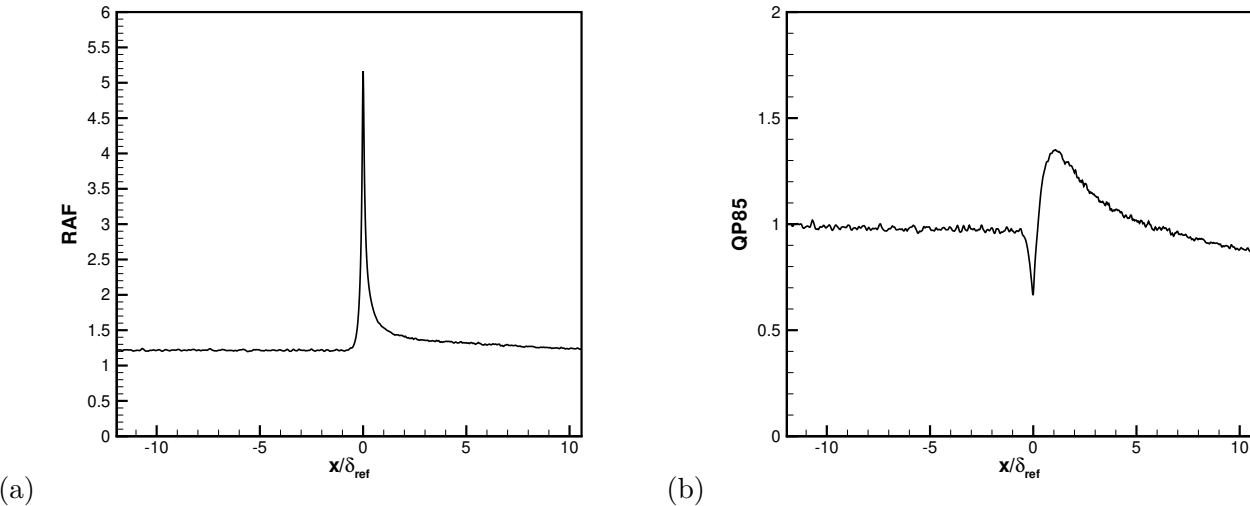


FIG. 28. Surface heat transfer scalings through the interaction: (a) Reynolds analogy, and (b) QP85 scaling.

The strong Reynolds analogy (SRA) links the temperature fluctuations T'' to the velocity fluctuations u'' (Morkovin [51]). According to the SRA, $R_{uT} = -\frac{\widetilde{u''T''}}{u''_{rms} T''_{rms}} \approx 1$ (phase relationship) and $\frac{1}{(\gamma-1)M^2} \frac{\tilde{u}}{u''_{rms}} \frac{T''_{rms}}{\tilde{T}} \approx 1$ (magnitude relationship). It is apparent from figure 29(a) that in the upstream boundary layer $R_{uT} \approx 0.6$ across most of the boundary layer as is typically seen in attached zero-pressure-gradient compressible boundary layers. The magnitude relation however is low at $0.5 - 0.8$ across the boundary layer. This is consistent with the observations of Duan et al. [36] and may be attributed to the cold wall temperature in the DNS. The modified SRA magnitude relation of Huang et al. [52], $\frac{1}{(\gamma-1)M^2} \frac{\tilde{u}}{u''_{rms}} \frac{T''_{rms}}{\tilde{T}} Pr_t \left(1 - \frac{\partial \tilde{T}_t}{\partial \tilde{T}}\right)$, accounts for the temperature effect and is close to unity across most of the upstream boundary layer (figure 29a). The most significant departures from the SRA occur in the near-wall region, between the wall and the location where the mean temperature \tilde{T} has a maximum (which is at $z/\delta \approx 0.02$ in the upstream boundary layer, see figure 15). The phase R_{uT} , for example, is negative near the wall, since $\frac{\partial \tilde{u}}{\partial z} > 0$ and $\frac{\partial \tilde{T}}{\partial z} > 0$ and hence u'' and T'' tend to be correlated rather than anti-correlated. The sign of $\frac{\partial \tilde{T}}{\partial z}$ changes at the wall-normal location where \tilde{T} has a maximum, so that above this location $\frac{\partial \tilde{T}}{\partial z} < 0$ and hence u'' and T'' are anti-correlated and R_{uT} is positive as typically observed. In the present attached STBLI, the departures from the SRA that are already present in the upstream boundary layer do not become significantly worse as the boundary layer interacts with the shock. As is apparent

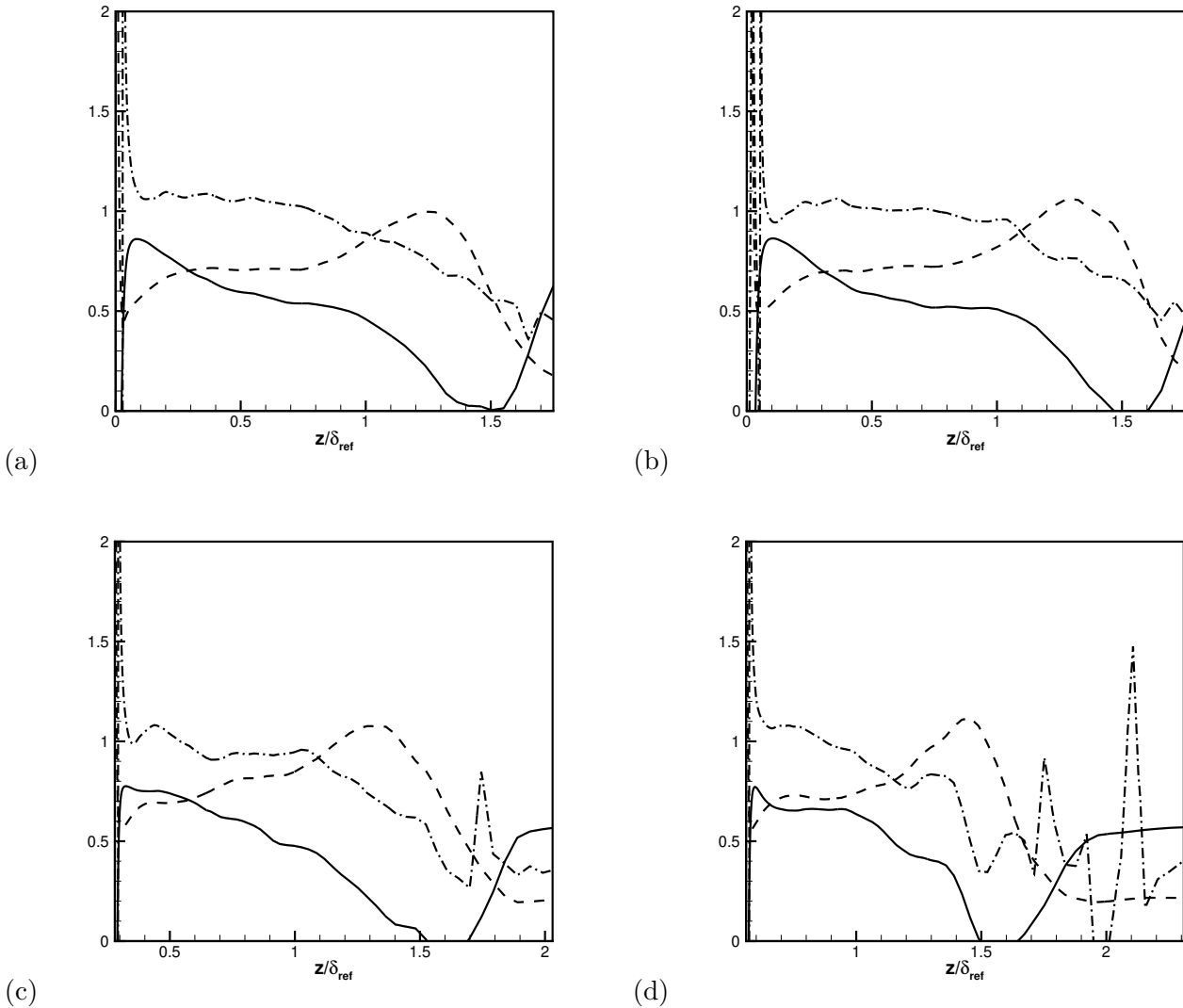


FIG. 29. Profiles of the SRA relations at various streamwise locations. SRA phase $R_{uT} = -\frac{\widetilde{u''T''}}{u''_{rms} T''_{rms}}$ (solid), SRA magnitude $\frac{1}{(\gamma-1)M^2} \frac{\tilde{u}}{u''_{rms}} \frac{T''_{rms}}{T}$ (dashed), and modified SRA magnitude $\frac{1}{(\gamma-1)M^2} \frac{\tilde{u}}{u''_{rms}} \frac{T''_{rms}}{T} Pr_t \left(1 - \frac{\partial \tilde{T}_t}{\partial T}\right)$ (dash-dot). (a) $x/\delta = -4.0$, (b) $x/\delta = 0.0$, (c) $x/\delta = 2.0$, and (d) $x/\delta = 4.0$.

from figures 29(b-d), over most of the boundary layer the phase relation remains around 0.6 through the interaction and the modified magnitude relation around unity. The profile shapes also remain generally similar downstream of the corner compared to the upstream boundary layer.

In turbulence models, the closure of the momentum equation is usually extended to the energy equation by assuming a constant turbulent Prandtl number: $Pr_t = \frac{\mu_t C_p}{\kappa_t} = const.$

In other words, the turbulent heat diffusivity κ_t is calculated from the eddy viscosity μ_t as $\kappa_t = (\mu_t C_p)/Pr_t$, where the turbulence model gives μ_t and Pr_t is usually taken to be close to 1. Figure 30 shows profiles of $Pr_t = \frac{\overline{\rho u'' w''}}{\overline{\rho T'' w''}} \frac{\partial \tilde{T}/\partial z}{\partial \tilde{u}/\partial z}$ at several streamwise locations through the interaction. Note that both in the calculation of the SRA relations shown in figure 29 and the turbulent Prandtl number shown in figure 30, for locations downstream of the corner, all velocity components and gradients have been taken in a ramp-aligned coordinate system (rotated by 8°). It is apparent that the assumption of a constant Pr_t close to 1 is satisfied reasonably well in most of the outer part of the boundary layer downstream of the corner. At $x/\delta = 4$, for example, Pr_t lies in the range 0.65 to 1.2 over most of the boundary layer.

However, as shown in figure 31, there are more significant differences near the wall. There is a ‘singularity’ with large departures from $Pr_t \approx 1$ at $z/\delta_{ref} = 0.025$ in the upstream boundary layer and at $(z - z_w)/\delta_{ref} = 0.013$ in the downstream boundary layer at $x/\delta_{ref} = 4.0$. This is due to the fact that \tilde{T} has a maximum, and as a result two of the terms that appear in the Pr_t definition, $\frac{\partial \tilde{T}}{\partial z}$ and $\overline{\rho T'' w''}$, are zero. The maximum of \tilde{T} is the result of two competing effects: the wall heat flux (cold wall) on the one hand and the viscous heating in the flow on the other. Above the wall-normal location of maximum \tilde{T} , Pr_t is approximately 1, whereas below that location, Pr_t is less than 1.

CONCLUSIONS

The hypersonic shock wave/turbulent boundary layer interaction generated by an 8° compression ramp in Mach 7.2 flow is investigated using DNS. The observed flow structure is different from that typically seen in supersonic interactions: at the present conditions, the shock angle is shallow (inviscid value 14.3°). This is typical for hypersonic flows, where the shock angle can be shallow and the layer extending from the wall to the shock can be thin, which is known as a thin shock layer (Anderson [53], pp. 13-14). As a result, the DNS shows that the shock foot is immersed in the boundary layer downstream of the corner for a streamwise distance equal to several incoming boundary layer thicknesses before it emerges from the boundary layer, distorted by the passage of the boundary layer structures.

While the flow is found to be attached in the mean, patches of separated flow are observed on an instantaneous basis surrounding the corner. Between $0.15\delta_{ref}$ upstream of the corner and $0.1\delta_{ref}$ downstream, the probability of reversed flow is greater than 20%, which means

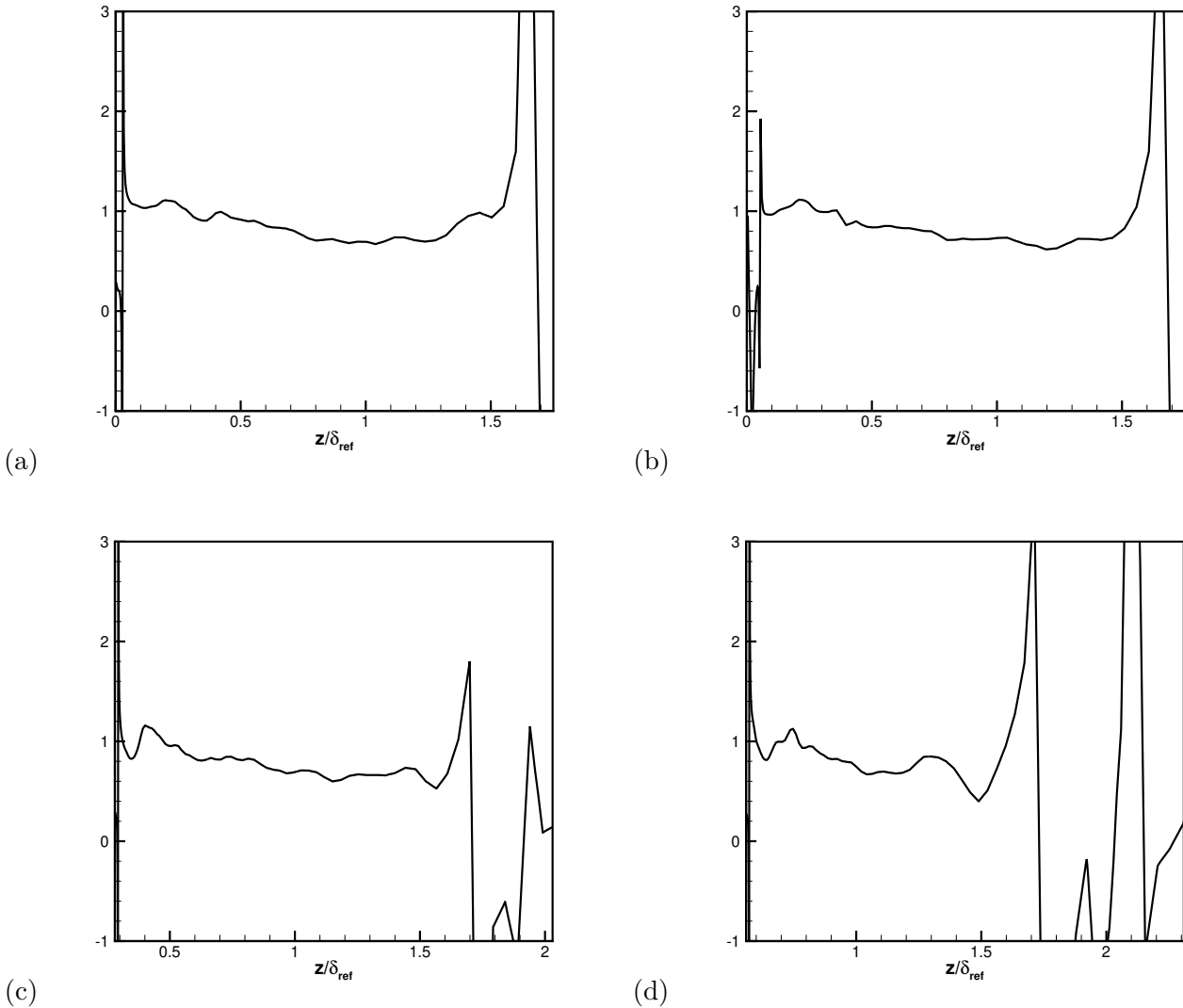


FIG. 30. Profiles of the turbulent Prandtl number $Pr_t = \frac{\overline{pu''w''}}{\rho T'' w''} \frac{\partial \tilde{T}}{\partial \tilde{u}}$ at various streamwise locations: (a) $x/\delta = -4.0$, (b) $x/\delta = 0.0$, (c) $x/\delta = 2.0$, and (d) $x/\delta = 4.0$.

that the flow is in the ITD (intermittent transitory detachment) state. The maximum probability is 31% at the corner.

The behavior of the turbulence through the interaction is described. The Reynolds stresses are amplified with the streamwise component being less amplified than the other two: R_{uu} is amplified by a factor of 1.82, R_{vv} by a factor of 2.53, R_{ww} by a factor of 2.28, and the shear stress R_{uw} by a factor of 2.12. The fluctuation peak remains close to the wall in the interaction, rather than moving away from the wall. This behavior is consistent with the fact that the low-speed region in the present flow is thin in the wall-normal direction:

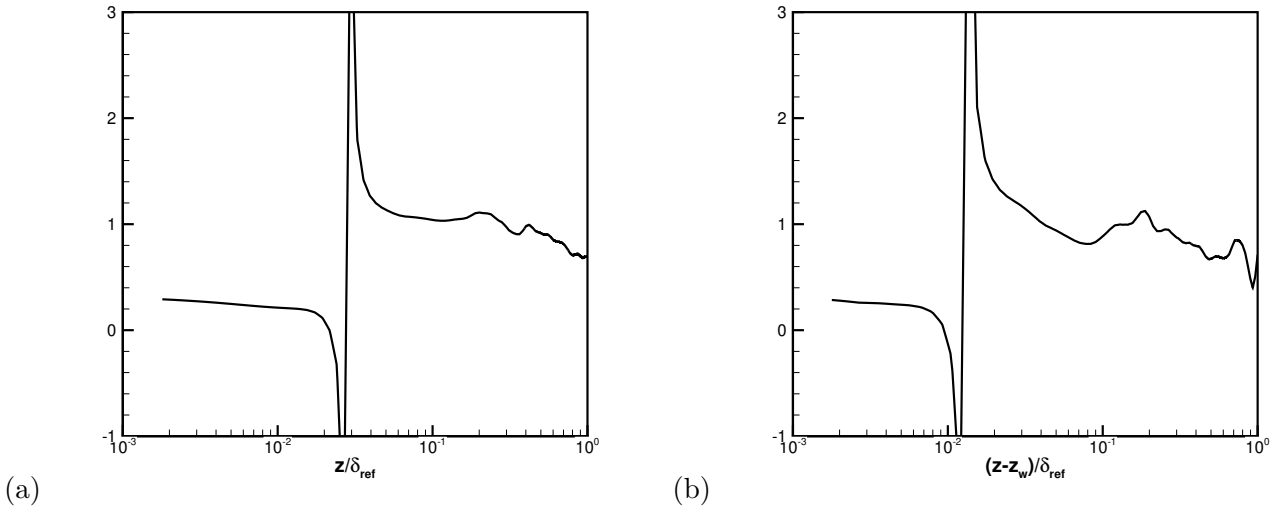


FIG. 31. Pr_t profiles on a semilog scale to highlight the near-wall behavior: (a) $x/\delta = -4.0$, and (b) $x/\delta = 4.0$.

the region of significant reversed flow probability does not extend above $z/\delta_{ref} \approx 0.05$, and the inflection point in the mean velocity profiles is found at similar wall-normal locations. The anisotropy of the Reynolds stresses changes through the interaction. In the upstream boundary layer, the Lumley triangles show the behavior typically seen in attached zero pressure gradient boundary layers. In the interaction region, however, a different structure is seen: both the second and third invariant of the Reynolds stress anisotropy tensor decrease (in other words, the invariant pair is pulled towards the origin), which is consistent with the turbulence becoming more isotropic.

Regarding the heat transfer, it is found that the Reynolds Analogy, which relates the skin friction coefficient C_f to the heat transfer coefficient C_h , is not satisfied in the interaction. Large values of the RA factor are observed at the corner, since the flow is close to separation and C_f approaches zero whereas C_h does not. The RA factor then remains above the range of values typically observed in zero-pressure-gradient hypersonic boundary layers for a significant distance downstream of the corner (up to $x/\delta_{ref} = 5.75$). As has previously been reported in the literature in the context of separated hypersonic STBLIs (e.g. Holden [12], Schülein [16], Murray et al. [17]), the heat transfer scales better with pressure, rather than skin friction, and the QP85 scaling of Back & Cuffel [18] describes the behavior in the DNS reasonably accurately, although there are departures from it near the corner. In the

present attached interaction, the departures from the SRA are relatively weak through the interaction, at least when compared to the behavior of the SRA terms in the upstream boundary layer and provided that the wall heat flux is taken into account by using a modified form of the SRA (Huang et al. [52]). The assumption of a constant turbulent Prandtl number around unity is also satisfied reasonably well, although significant departures from it are observed in the near-wall region.

The present DNS data are compared to available experiments, and a good qualitative match is found in terms of the instantaneous and mean flow structure, as well as for the state of separation.

We expect the DNS to be useful for turbulence modeling, given the known deficiencies of turbulence models in hypersonic STBLIs even for attached cases (see Gnoffo et al. [21], Roy & Blottner [20], Brown [22]). In the present work, we provide quantities relevant for turbulence modeling, such as mean and fluctuating fields, Reynolds stresses, the anisotropy tensor, TKE budgets, and the turbulent Prandtl number.

This work was supported by the Air Force Office of Scientific Research under grant numbers FA9550-09-1-0464 and FA9550-17-1-0104.

* Present address: GE Research, Niskayuna NY 12309

- [1] V. Mikulla and C. C. Horstman, “Turbulence measurements in hypersonic shock-wave boundary-layer interaction flows,” *AIAA Journal* **14**, 568–575 (1976).
- [2] P. B. Bookey, C. Wyckham, A. J. Smits, and M. P. Martin, “New Experimental Data of STBLI at DNS/LES Accessible Reynolds Numbers,” *AIAA Paper No. 2005-309* (2005).
- [3] A.-M. Schreyer, D. Sahoo, and A. J. Smits, “Experimental investigations of a hypersonic shock turbulent boundary layer interaction,” *AIAA* (2011), paper 2011-481.
- [4] A.-M. Schreyer, D. Sahoo, O. J. H. Williams, and A. J. Smits, “Experimental investigation of two hypersonic shock/turbulent boundary-layer interactions,” *AIAA Journal* **56**, 4830–4844 (2018).
- [5] F. F. J. Schrijer, F. Scarano, and B. W. van Oudheusden, “Application of PIV in a Mach 7 double-ramp flow,” *Experiments in Fluids* **41**, 353–363 (2006).
- [6] J. Brooks, A. K. Gupta, C. Helm, M. P. Martín, M. Smith, and E. Marineau, “Mach 10 PIV

- Flow Field Measurements of a Turbulent Boundary Layer and Shock Turbulent Boundary Layer Interaction,” (2017) paper no. AIAA 2017-3325.
- [7] G. M. Elfstrom, “Turbulent hypersonic flow at a wedge-compression corner,” Journal of Fluid Mechanics **53**, 113–127 (1972).
 - [8] G. T. Coleman and J. L. Stollery, “Heat transfer from hypersonic turbulent flow at a wedge compression corner,” Journal of Fluid Mechanics **56**, 741–752 (1972).
 - [9] M. I. Kussoy and C. C. Horstman, *An experimental documentation of a hypersonic shock-wave turbulent boundary layer interaction flow – with and without separation*, Tech. Rep. TM X-62412 (NASA, 1975).
 - [10] M. I. Kussoy and C. C. Horstman, *Documentation of Two- and Three-Dimensional Hypersonic Shock Wave/Turbulent Boundary Layer Interaction Flows*, Tech. Rep. TM 101075 (NASA, 1989).
 - [11] M. I. Kussoy and C. C. Horstman, *Documentation of Two- and Three-Dimensional Shock-Wave/Turbulent-Boundary-Layer Interaction Flows at Mach 8.2*, Tech. Rep. TM 103838 (NASA, 1991).
 - [12] M. S. Holden, *Shock Wave Turbulent Boundary Layer Interaction in Hypersonic Flow*, Tech. Rep. ARL TR 75-0204 (Aerospace Research Laboratories, 1975).
 - [13] M. S. Holden, “Studies of the Mean and Unsteady Structure of Turbulent Boundary Layer Separation in Hypersonic Flow,” (1991) paper no. AIAA 91-1778.
 - [14] M. S. Holden, J. R. Moselle, S. J. Sweet, and S. C. Martin, “A Database of Aerothermal Measurements in Hypersonic Flow for CFD Validation,” (1996) paper no. AIAA 96-4597.
 - [15] M. Holden, M. MacLean, T. Wadhams, and E. Mundy, “Experimental studies of shock wave/turbulent boundary layer interaction in high Reynolds number supersonic and hypersonic flows to evaluate the performance of CFD codes,” (2010) paper no. AIAA 2010-4468.
 - [16] E. Schülein, “Skin-friction and heat flux measurements in shock/boundary-layer interaction flows,” AIAA Journal **44**, 1732–1741 (2006).
 - [17] N. Murray, R. Hillier, and S. Williams, “Experimental investigation of axisymmetric hypersonic shock-wave/turbulent-boundary-layer interactions,” Journal of Fluid Mechanics **714**, 152–189 (2013).
 - [18] L. H. Back and R. F. Cuffel, “Changes in heat transfer from turbulent boundary layers interacting with shock waves and expansion waves,” AIAA J. **8**, 1871–1873 (1970).

- [19] D. V. Gaitonde, “Progress in shock wave/boundary layer interactions,” *Progress in Aerospace Sciences* **72**, 80–99 (2015).
- [20] C. J. Roy and F. G. Blottner, “Review and assessment of turbulence models for hypersonic flows,” *Progress in Aerospace Sciences* **42**, 469–530 (2006).
- [21] P. A. Gnoffo, S. A. Berry, and J. W. Van Norman, “Uncertainty assessments of 2D and axisymmetric hypersonic shock wave - turbulent boundary layer interaction simulations at compression corners,” 42nd AIAA Thermophysics Conference (2011), paper 2011-3142.
- [22] J. L. Brown, “Shock wave impingement on boundary layers at hypersonic speeds: computational analysis and uncertainty,” 42nd AIAA Thermophysics Conference (2011), paper 2011-3143.
- [23] D. Knight and M. Mortazavi, *Simulation of non-equilibrium hypersonic shock wave boundary layer interactions using the Navier–Stokes equations*, Tech. Rep. CCD Report 2018-1 (Rutgers University, 2018).
- [24] G. S. Settles and L. J. Dodson, *Hypersonic shock/boundary-layer interaction database*, Tech. Rep. CR-177577 (NASA, 1991).
- [25] G. S. Settles and L. J. Dodson, *Hypersonic shock/boundary-layer interaction database: new and corrected data*, Tech. Rep. CR-177638 (NASA, 1994).
- [26] G. S. Settles and L. J. Dodson, “Supersonic and hypersonic shock/boundary-layer interaction database,” *AIAA Journal* **32**, 1377–1383 (1994).
- [27] M. P. Martín, E. M. Taylor, M. Wu, and V. G. Weirs, “A bandwidth-optimized WENO scheme for the effective direct numerical simulation of compressible turbulence,” *Journal of Computational Physics* **220**, 270–289 (2006).
- [28] E. M. Taylor, M. Wu, and M. P. Martín, “Optimization of nonlinear error for weighted essentially non-oscillatory methods in direct numerical simulations of compressible turbulence,” *Journal of Computational Physics* **223**, 384–397 (2007).
- [29] J. H. Williamson, “Low-storage Runge–Kutta schemes,” *Journal of Computational Physics* **35**, 48 – 56 (1980).
- [30] F. G. Keyes, “A summary of viscosity and heat-conduction data for He , A , H_2 , O_2 , N_2 , CO , CO_2 , H_2O , and air,” *Transactions of the American Society of Mechanical Engineers* **73**, 589–596 (1951).
- [31] S. Xu and M. P. Martín, “Assessment of inflow boundary conditions for compressible turbulent

- boundary layers,” Physics of Fluids **16**, 2623–2639 (2004).
- [32] M. Wu and M. P. Martín, “Direct numerical simulation of supersonic turbulent boundary layer over a compression ramp,” AIAA Journal **45**, 879–889 (2007).
- [33] M. Ringuette, M. Wu, and M. P. Martín, “Low Reynolds number effects in a Mach 3 shock/turbulent-boundary-layer interaction,” AIAA Journal **46**, 1884–1887 (2008).
- [34] S. Priebe, M. Wu, and M. P. Martín, “Direct numerical simulation of a reflected-shock-wave/turbulent-boundary-layer interaction,” AIAA Journal **47**, 1173–1185 (2009).
- [35] M. P. Martín, “Direct numerical simulation of hypersonic turbulent boundary layers. Part 1. Initialization and comparison with experiments,” Journal of Fluid Mechanics **570**, 347–364 (2007).
- [36] L. Duan, I. Beekman, and M. P. Martín, “Direct numerical simulation of hypersonic turbulent boundary layers. Part 2. Effect of wall temperature,” Journal of Fluid Mechanics **655**, 419–445 (2010).
- [37] L. Duan, I. Beekman, and M. P. Martín, “Direct Numerical Simulation of Hypersonic Turbulent Boundary Layers. Part III: Effect of Mach Number,” Journal of Fluid Mechanics **672**, 245–267 (2011).
- [38] S. Priebe, *Direct Numerical Simulation of Two Shock Wave/Turbulent Boundary Layer Interactions*, Ph.D. thesis, Princeton University (2012).
- [39] S. Priebe and M. P. Martín, “Direct numerical simulation of a hypersonic turbulent boundary layer on a large domain,” (2011) paper no. AIAA 2011-3432.
- [40] R. L. Simpson, “Turbulent Boundary-Layer Separation,” Annual Review of Fluid Mechanics **21**, 205–234 (1989).
- [41] Y. Na and P. Moin, “Direct numerical simulation of a separated turbulent boundary layer,” Journal of Fluid Mechanics **374**, 379–405 (1998).
- [42] S. Pirozzoli, M. Bernardini, and F. Grasso, “Direct numerical simulation of transonic shock/boundary layer interaction under conditions of incipient separation,” Journal of Fluid Mechanics **657**, 361–393 (2010).
- [43] S. Piponnai, J. P. Dussauge, J. F. Debièvre, and P. Dupont, “A simple model for low-frequency unsteadiness in shock-induced separation,” Journal of Fluid Mechanics **629**, 87–108 (2009).
- [44] J. L. Lumley and G. R. Newman, “The return to isotropy of homogeneous turbulence,” Journal

- of Fluid Mechanics **82**, 161–178 (1977).
- [45] K.-S. Choi and J. L. Lumley, “The return to isotropy of homogeneous turbulence,” Journal of Fluid Mechanics **436**, 59–84 (2001).
- [46] S. B. Pope, *Turbulent Flows* (Cambridge University Press, 2000).
- [47] M. Grilli, S. Hickel, and N. A. Adams, “Large-eddy simulation of a supersonic turbulent boundary layer over a compression-expansion ramp,” International Journal of Heat and Fluid Flow **42**, 79–93 (2013).
- [48] J.-P. Dussauge, P. Dupont, and J.-F. Debièvre, “Unsteadiness in shock wave boundary layer interactions with separation,” Aerospace Science and Technology **10**, 85–91 (2006).
- [49] N. T. Clemens and V. Narayanaswamy, “Low-frequency unsteadiness of shock wave/turbulent boundary layer interactions,” Annual Review of Fluid Mechanics **46**, 469–492 (2014).
- [50] D. C. Wilcox, *Turbulence Modeling for CFD*, 3rd ed. (DCW Industries, 2006).
- [51] M. V. Morkovin, “Effects of compressibility on turbulent flows,” in *Mécanique de la Turbulence* (1962) pp. 367–380.
- [52] P. G. Huang, G. N. Coleman, and P. Bradshaw, “Compressible turbulent channel flows: DNS results and modelling,” Journal of Fluid Mechanics **305**, 185–218 (1995).
- [53] J. D. Anderson, *Hypersonic and high-temperature gas dynamics*, 2nd ed. (AIAA Education Series, 2006).